

AD-785 180

FREQUENCY TUNED CO₂ LASER

R. L. Abrams, et al

Hughes Research Laboratories

Prepared for:

Office of Naval Research
Advanced Research Projects Agency

August 1974

DISTRIBUTED BY:

NTIS

National Technical Information Service
U. S. DEPARTMENT OF COMMERCE
5285 Port Royal Road, Springfield Va. 22151

UNCLASSIFIED

SECURITY CLASSIFICATION OF THIS PAGE (When Data Entered)

AD 785180

REPORT DOCUMENTATION PAGE		READ INSTRUCTIONS BEFORE COMPLETING FORM
1. REPORT NUMBER N00014-73-C-0324 ✓	2. GOVT ACCESSION NO.	3. RECIPIENT'S CATALOG NUMBER
4. TITLE (and Subtitle) FREQUENCY TUNED CO ₂ LASER		5. TYPE OF REPORT & PERIOD COVERED Final Technical Report 19 March 73 - 30 June 74
		6. PERFORMING ORG. REPORT NUMBER
7. AUTHOR(s) R. L. Abrams and M. B. Klein		8. CONTRACT OR GRANT NUMBER(s) N00014-73-C-0324
9. PERFORMING ORGANIZATION NAME AND ADDRESS Hughes Research Laboratories 3011 Malibu Canyon Road Malibu, CA 90265		10. PROGRAM ELEMENT, PROJECT, TASK AREA & WORK UNIT NUMBERS
11. CONTROLLING OFFICE NAME AND ADDRESS Advanced Research Projects Agency Arlington, Virginia 22209		12. REPORT DATE August 1974
14. MONITORING AGENCY NAME & ADDRESS (if different from Controlling Office)		13. NUMBER OF PAGES 106
		15. SECURITY CLASS. (of this report) Unclassified
16. DISTRIBUTION STATEMENT (of this Report)		
17. DISTRIBUTION STATEMENT (of the abstract entered in Block 20, if different from Report)		
18. SUPPLEMENTARY NOTES		
19. KEY WORDS (Continue on reverse side if necessary and identify by block number) Waveguide Laser, Tunable CO ₂ Laser, Tunable Local Oscillator, CO ₂ Waveguide Laser <div style="text-align: right;">Reproduced by NATIONAL TECHNICAL INFORMATION SERVICE U S Department of Commerce Springfield VA 22151</div>		
20. ABSTRACT (Continue on reverse side if necessary and identify by block number) This program represents an effort to exploit the advantages of waveguide laser technology for the development of advanced components suitable for optical radar applications. These include a CO ₂ laser local oscillator, tunable ±750 MHz from line center for heterodyne detection of doppler shifted signals, and an intermediate level power amplifier with ~20 dB of saturated gain, 100 to 200 W of output power, and 500 MHz dynamic bandwidth. Conventional CO ₂ lasers are incapable of satisfying these		

UNCLASSIFIED

SECURITY CLASSIFICATION OF THIS PAGE(When Data Entered)

requirements because of their limited gain linewidth. Waveguide CO₂ laser devices, however, operate at elevated gas pressures, where collision broadening of the laser transition provides the desired increased gain bandwidth.

A parametric study of tunable waveguide lasers is described in which tube geometry, gas mixture, and mirror mount design were all varied to determine the optimum design for frequency tunability and stability. The final device consists of a 1.0-mm square by 9.5-cm long waveguide laser with 80 mW output power, 1.2 GHz tunability, and <10 kHz short term frequency stability, all achieved under sealed-off conditions. Although these numbers fall somewhat short of the program goals (1.5 GHz tunability, 100 mW output, and <1 kHz frequency stability), they represent the state of the art in tunable CO₂ laser technology.

A 1.65 mm i.d. x 1 m waveguide amplifier test bed was constructed with an active gain length of 77 cm. The device consists of 7 BeO ceramic sections, each of which is 5 in. long. The segments are joined with epoxy to metal flanges at each end. Each section is water cooled, and is supplied with flowing gas from the end flanges. We have measured small signal gain and saturation power in this device for a variety of experimental conditions. On the basis of these measurements, we discuss the specific trade-offs involved in designing a full scale device which achieves the required output power and bandwidth. We find an optimum pressure of 100 Torr, and a required length which varies from 3 m (for 17 dB overall gain) to 7 m (for 23 dB overall gain).

UNCLASSIFIED

SECURITY CLASSIFICATION OF THIS PAGE(When Data Entered)

TABLE OF CONTENTS

	LIST OF ILLUSTRATIONS	vii
	ABSTRACT	ix
	FOREWORD	xi
I	INTRODUCTION AND SUMMARY	1
II	TUNABLE LOCAL OSCILLATOR	5
	A. Preliminary Experiments	5
	B. Laser Fabrication	8
	C. Power Measurements	14
	D. Tuning Experiments	18
	E. Final Design and Performance	26
III	WAVEGUIDE POWER AMPLIFIER	35
	A. Summary	35
	B. Waveguide Amplifier Theory	35
	C. Test Bed Description	44
	D. Gas Flow Considerations	47
	E. Electrical Circuitry	50
	F. Experimental Results	54
	G. Characterization of Full Scale Device	61
	REFERENCES	67
	APPENDICES	
	A — Waveguide Losses	69
	B — Gigahertz Tunable Waveguide CO ₂ Laser	93

Page iv is Blank,

LIST OF ILLUSTRATIONS

FIGURE		PAGE
1	Test section for multiple electrode geometry	6
2	Construction details of tunable laser	9
3	Pieces used to fabricate 1.0 mm square bore tube	10
4	Adjustment device mounted on a square bore tube	12
5	Laser output and bimorph voltage	13
6	Tunable laser	15
7	Output power versus gas pressure for tube A-20	16
8	Output power versus gas pressure for tube A-22	17
9	Experimental arrangement for tuning range measurements	19
10	Laser output versus bimorph tuning for tube A-18	20
11	Tuning characteristics of tube A-20	22
12	Observed tuning range and output power versus pressure for tube A-20	23
13	Tuning characteristic of tube A-20	24
14	Tuning characteristic of tube A-22	25
15	Photograph of 1.0 mm square waveguide laser in final form	27
16	Laser output power versus bimorph tuning for tube A-23	28
17	Laser starting circuit	29

FIGURE		PAGE
18	Experimental arrangement for frequency stability measurements	31
19	Spectrum analyzer displays of beat frequency	32
20	Output of frequency discriminator when beat frequency is set at 30 MHz	33
21	Normalized output linewidth versus normalized output intensity for several values of overall gain	39
22	Normalized line profiles for $G = 10$ dB (upper) and $G = 50$ dB (lower)	40
23	Double-pass amplifier configuration	41
24	Amplifier assembly	45
25	Detail of electrical and gas flow connections	46
26	Completed amplifier	48
27	Schematic diagram of gas flow system	49
28	Schematic diagram of electrical connections	52
29	Schematic diagram of starter circuit	53
30	Gain versus flowrate for 50,000 and 150 Torr pressure	56
31	Gain versus pressure at constant flow rate and current	57
32	Graphical technique for measuring saturation power	59
33	Saturation power and intensity versus pressure flow rate = 500 changes/s	60
34	Available output power and input electrical power versus pressure	62
35	Required length as a function of output power for a 1 W input	64

ABSTRACT

This program represents an effort to exploit the advantages of waveguide laser technology for the development of advanced components suitable for optical radar applications. These include a CO_2 laser local oscillator, tunable ± 750 MHz from line center for heterodyne detection of doppler shifted signals, and an intermediate level power amplifier with ~ 20 dB of saturated gain, 100 to 200 W of output power, and 500 MHz dynamic bandwidth. Conventional CO_2 lasers are incapable of satisfying these requirements because of their limited gain line-width. Waveguide CO_2 laser devices, however, operate at elevated gas pressures, where collision broadening of the laser transition provides the desired increased gain bandwidth.

A parametric study of tunable waveguide lasers is described in which tube geometry, gas mixture, and mirror mount design were all varied to determine the optimum design for frequency tunability and stability. The final device consists of a 1.0-mm square by 9.5-cm long waveguide laser with 80 mW output power, 1.2 GHz tunability, and < 10 kHz short term frequency stability, all achieved under sealed-off conditions. Although these numbers fall somewhat short of the program goals (1.5 GHz tunability, 100 mW output, and < 1 kHz frequency stability), they represent the state of the art in tunable CO_2 laser technology.

A 1.65 mm i.d. x 1 m waveguide amplifier test bed was constructed with an active gain length of 77 cm. The device consists of 7 BeO ceramic sections, each of which is 5-in. long. The segments are joined with epoxy to metal flanges at each end. Each section is water cooled, and is supplied with flowing gas from the end flanges. We have measured small signal gain and saturation power in this device for a variety of experimental conditions. On the basis of these measurements we discuss the specific trade-offs involved in designing a full scale device which achieves the required output power and bandwidth. We find an optimum pressure of 100 Torr, and a required length which varies from 3 m (for 17 dB overall gain) to 7 m (for 23 dB overall gain).

FOREWORD

The research reported here was accomplished with the advice and aid of the following people: H. R. Friedrich and R. E. Brower were primarily responsible for mechanical design and construction of the laser tubes, while M. B. Klein and G. Tangonan performed the analysis and experiments leading to an understanding of the mechanism for guide loss due to rough surfaces. M. B. Klein was responsible for the analysis and experimental results performed on the waveguide power amplifier. G. N. Rupert aided M. B. Klein in the power amplifier work and was responsible for design and testing of the laser starting circuit.

I. INTRODUCTION AND SUMMARY

Modern optical radar systems for surveillance of orbiting objects require a number of specialized components which can best be developed using waveguide laser technology. These include a CO₂ laser local oscillator, tunable ± 750 MHz from line center for heterodyne detection of doppler shifted signals, and an intermediate level power amplifier with ~ 20 dB of saturated gain, 100 to 200 W of output power, and 500 MHz of dynamic bandwidth. Conventional CO₂ laser devices are incapable of satisfying these requirements because of their limited gain linewidth. In order to increase the linewidth of CO₂ laser devices, it is necessary to raise the laser operating pressure, thereby broadening the laser transition by collisions. The linewidth of a typical CO₂ gas mixture at room temperature increases at a rate of ~ 5.3 MHz/Torr and equals 1500 MHz at a pressure of 283 Torr.

It has previously been demonstrated¹ at Hughes Research Laboratories that high pressure operation (above 300 Torr) of CO₂ lasers can be achieved under sealed-off conditions by operating the laser in the waveguide configuration. The discharge diameter of the laser must be decreased as the pressure is increased, and increasing optical diffraction losses are avoided by using the narrow bore capillary as a hollow optical waveguide.²

The approach undertaken in this program is to develop the concept of a sealed-off waveguide CO₂ laser in order to achieve as large a tuning range as possible. Sealed-off operation was specified in the interest of frequency stability. Since frequency stability is less important in the waveguide power amplifier, a flowing gas device was chosen for the higher available gain.³

A parametric study of tunable waveguide lasers is described in this report. Tube diameter, gas mixture, pressure, and mirror mount design were all varied to determine the optimum design for frequency tunability and stability. The final device represents the best room temperature, sealed-off, tunable device available. Output power of 80 mW, tunability of 1.2 GHz, and short term frequency stability of

better than 10 kHz are all achieved in a sealed-off device to be delivered to a laboratory designated by the contracting officer. Although these numbers fall somewhat short of the program goals (1.5 GHz tunability, 100 mW output, and <1 kHz frequency stability), they represent the state of the art in tunable CO₂ laser technology. It is because of the efforts exerted in this program that such a sophisticated high performance device is now available.

The development of a waveguide power amplifier with 500 MHz bandwidth and ~ 20 dB gain will permit a large cost and size reduction in a high power amplifier chain. The purpose of this program was to perform the necessary analysis to theoretically characterize a waveguide power amplifier (gain, power, bandwidth) and to carry out measurements on a 1 m test section. The ultimate goal of the program is to demonstrate feasibility and to obtain data necessary to confidently design a power amplifier, given requirements for saturated gain, power output, and bandwidth.

The amplifier test bed which was constructed for the program is 98-cm long with an active length of 77 cm. The waveguide diameter is 1.65 mm, and is composed of a number of BeO sections with parallel gas flow and multiple electric discharge paths. Measurements of gain and saturation intensity on this device are described in Section III of this report. It is shown that a 200 W output, 500 MHz bandwidth amplifier, with 23 dB gain should operate at 100 Torr pressure and will be 7.5-m long. The required length is longer than originally expected, primarily because the measured saturation intensity is smaller than values reported for sealed-off tubes. It may turn out that a 100 W output may be preferred from a total systems point of view. Some improvement in these numbers will also be achieved by cooling of the structure to dry ice temperature.

The progress and performance of the tunable local oscillator is discussed in Section II. In Section III, the analytical as well as the experimental results on the power amplifier are presented. Two appendices are included. Appendix A contains an analysis along with experimental results on the effects of surface roughness on waveguide

loss. Appendix B contains a reprint of a paper to be published in the Sept. 1974 issue of Applied Physics Letters, describing the tunable laser research.

II. TUNABLE LOCAL OSCILLATOR

A. Preliminary Experiments

Two crucial experiments were performed early in the program to prove out concepts which we proposed for the tunable laser. These related to electrode geometry and the use of a diffraction grating for line selection.

The proposed electrode geometry is similar to that shown in Fig. 1. The advantage of such a configuration is that both ends of the laser can be at ground potential (although this is not shown in Fig. 1), which simplifies the electrical circuitry for the bender bimorph and also has a safety advantage. Operation with negative high voltage allows the cathodes (center electrodes) to be removed from the optics, avoiding problems with sputtering damage to the mirrors.

In order to test the above concept, the test section shown in Fig. 1 was fabricated. The tube consists of a BeO bore, 8.5 cm x 1.0 mm i.d., and the electrodes are hollow nickel pins. It was found that all four discharge paths could be simultaneously excited at pressures up to 300 Torr. When the high voltage was increased slowly, some paths would not light, but when turned up suddenly, all paths usually light simultaneously. At pressures above 200 Torr, however, several attempts were necessary in order to light all paths. It should be a simple matter to start all paths together with either a Tesla coil or a high voltage pulse for a final power supply design. A high voltage pulse starting circuit has been developed for this purpose and is described in Section III.

The use of a diffraction grating in a waveguide laser places some severe requirements on the grating. It must possess a Littrow diffraction efficiency high enough (above 95%) to be used in these low gain lasers and must be capable of withstanding very high power densities ($> 1 \text{ kW/cm}^2$). Our past experience has shown that some replica gratings have efficiencies greater than 95% when overcoated with gold, but damage occurred when used as reflectors in conventional lasers. We have found, however, that if the replica is mounted on copper, rather

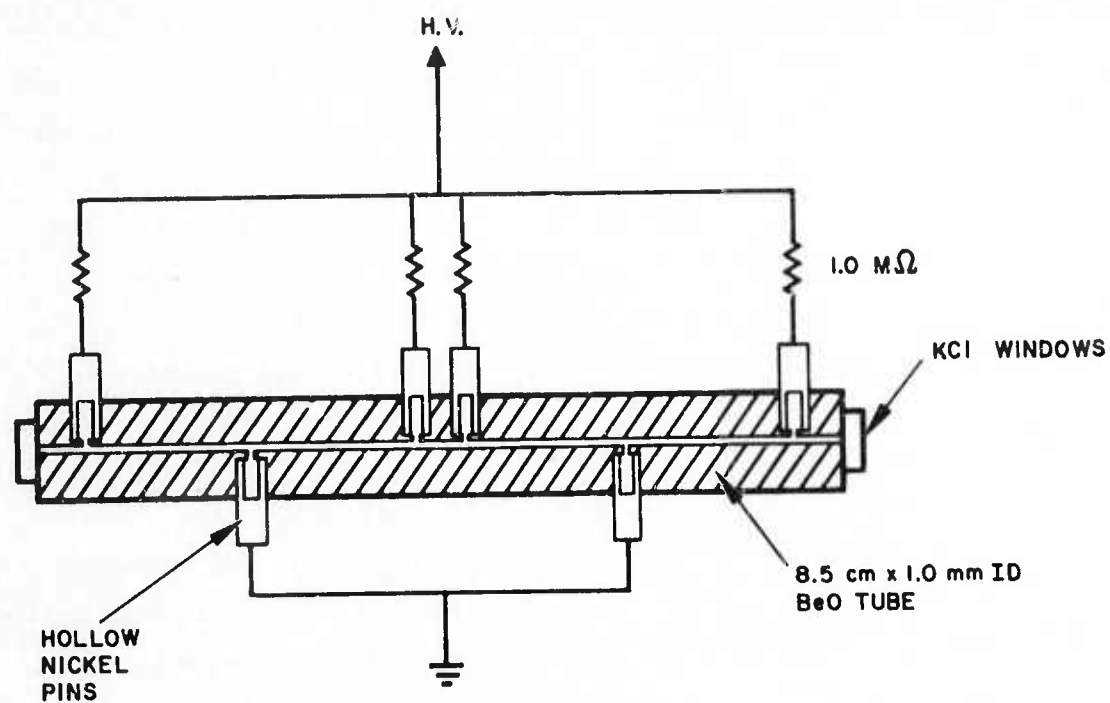


Fig. 1. Test section for multiple electrode geometry.

than glass, the increased thermal conductance prevents damage. For this reason, we acquired a Bausch and Lomb No. 35-53-04-890, 150 l/mm, 8/ μ m blaze grating mounted on a copper substrate.

Careful measurements of Littrow reflectivity for this grating at 10.6 μ m showed a reflectance of 97% for the polarization normal to the grating grooves and 20.5% for the polarization parallel to the grooves. Thus, when used as a reflector, the grating acts as a polarization selector as well as a line selector. The energy reflected specularly for the 97% Littrow orientation was 0.6%, so more than 2% of the energy is dissipated or scattered.

We found that if these gratings were covered with a commercial strippable protective covering, they could be cut with a cutting wheel and the reflectivity was unchanged after the coating was removed. In this manner, a number of gratings usable for waveguide lasers were obtained from a single purchased grating.

An adjustable mount was fabricated to test one of the cut pieces in a 1.5 mm square x 10 cm Al_2O_3 waveguide CO_2 laser. The laser produced ~ 0.6 W on P(20) of the 00^0_1 to 10^0_1 transition, about half the power expected with a total reflector replacing the grating. This is consistent with the fact that the 3% loss from the grating is close to the 4% loss on the output mirror. We were able to select a number of transitions with this fixture. No damage was observed on the diffraction grating after operation for several hours.

The results of this experiment show that the diffraction grating is a suitable optical element for waveguide lasers. Although the diffraction efficiency (97%) achieved is impressive, it is clear that the goals of this program would be better served if a grating with higher efficiency were available. An attempt to fabricate such a grating is being made here at Hughes Research Laboratories.

In a preliminary experiment, Dr. H.L. Garvin showed that it was possible to ion machine sawtooth-shaped grooves in germanium and other materials. In an attempt to make a blazed grating, a 12- μ m line spacing was machined in a ZnS coated glass blank. After overcoating with gold, this grating had a measured Littrow efficiency of 95%.

Even more impressive was the fact that no energy was measured in zero order ($<0.1\%$), so considerable energy was lost to absorption and scatter. Since the ZnS was polycrystalline, it is believed that a higher quality grating can be machined in a single crystal surface. In the future we hope to fabricate such a grating in germanium. In addition to the potentially high efficiency, these gratings should be capable of handling large power densities, as they will have no replicating layer to act as thermal isolation for the reflecting surface.

With the successful completion of the above preliminary experiments, the fabrication of lasers for tunable local oscillator experiments was initiated.

B. Laser Fabrication

Two basic types of hollow waveguide lasers were fabricated for use in this program, namely those with hollow circular and hollow square cross sections. Fundamentally different approaches were taken for tube fabrication, but the hardware for mounting and adjusting optics were the same. Three sizes of waveguide lasers were tested, 1.5 mm circular bore, 1.0 mm square bore, and 0.75 mm square bore. The fabrication of these tubes is discussed in the following paragraphs.

The construction of the 1.5 mm i.d. circular bore laser is discussed with reference to Fig. 2. The body of the laser consists of a 1 in. o.d. \times 9.5-cm long BeO rod. A 1.5-mm hole is drilled the length of the rod, and counterbored holes are provided from the sides for electrodes as shown. Kovar sleeves are brazed to the BeO ends which have been metallized. Copper gasketed vacuum flanges are welded to the sleeves and all subsequent hardware is mounted by means of mating flanges.

All of the square bore lasers are fabricated from polished BeO slabs, 9.5-cm long, epoxied together to form a square waveguide. In this case, the copper gasketed flanges are machined to fit over the rectangular outer dimensions of the tube, and are epoxy sealed. A photograph of the pieces used to fabricate these tubes is shown in Fig. 3.

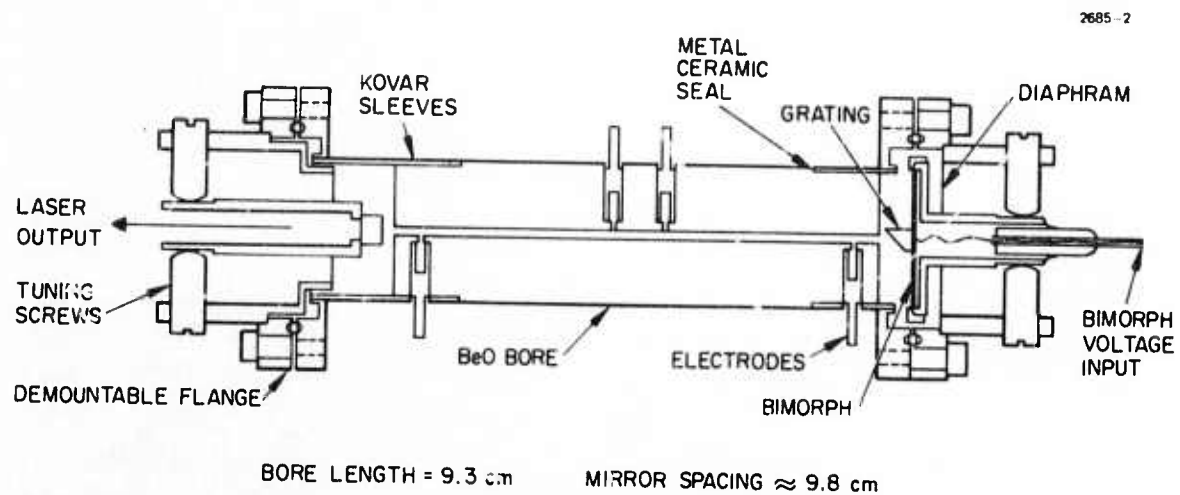


Fig. 2. Construction details of tunable laser.

M10138

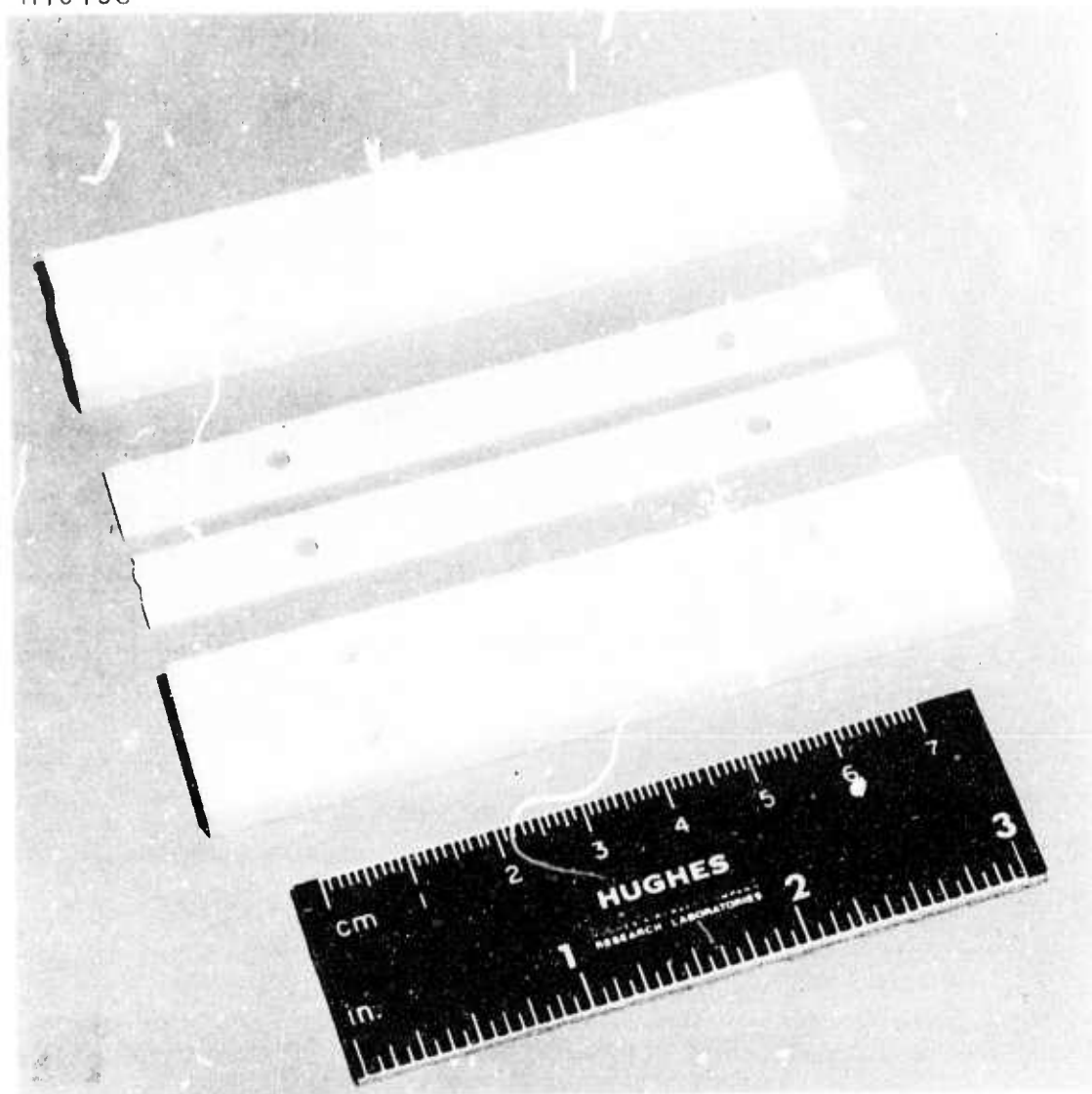


Fig. 3. Pieces used to fabricate 1.0 mm square bore tube.

Two types of special flange mounted mirror alignment devices have been designed and built for these tubes. In one design, the mirror holder and the bender bimorph device are mounted on a post which is brazed through a 0.010-in. stainless steel diaphragm. Adjustments of the mirror or grating alignment are made by turning the adjusting screws and flexing the diaphragm. The grating and mirror are epoxied to their respective holders and the bender bimorph is held against a nylon retaining ring by a threaded holder. The electrical connection to the bimorph is made through a ceramic feedthrough through the end of the adjustment device.

Frequency stability measurements revealed that the stainless steel diaphragm was susceptible to microphonic pickup and mechanical resonance. A different type of adjustment device was designed and fabricated and is shown in Fig. 4, mounted on a square bored tube. The flexible vacuum seal is accomplished by means of a stainless steel bellows, and adjustments are made with four screws, which can be tightened to lock the mirror alignment in a ball and socket type mount. This mount has proven to be smoother and more stable than the diaphragm type mount.

The bender bimorph is a one inch circular disc, 0.020-in. thick and is composed of two oppositely poled piezoelectric discs, bonded together. Application of a voltage across the bimorph causes the 1-in. disc to buckle slightly, resulting in a linear motion at the center of the disc, normal to its plane. The bimorph holder serves to clamp the disc at its edge and provides for electrical connection.

A 2.0 mm x 10 cm waveguide laser was fitted with a totally reflecting mirror mounted on the bimorph and a 96% reflecting output mirror. A linear ramp voltage was applied to the bimorph, and the ramp as well as laser output is displayed in Fig. 5. The ramp height is 210 V and 9 orders (or half wavelengths) are displayed. Thus, the average sensitivity of the bimorph is $0.28 \mu\text{m}/\text{V}$ and about 23 V are required to tune the laser over one order ($5.3 \mu\text{m}$).

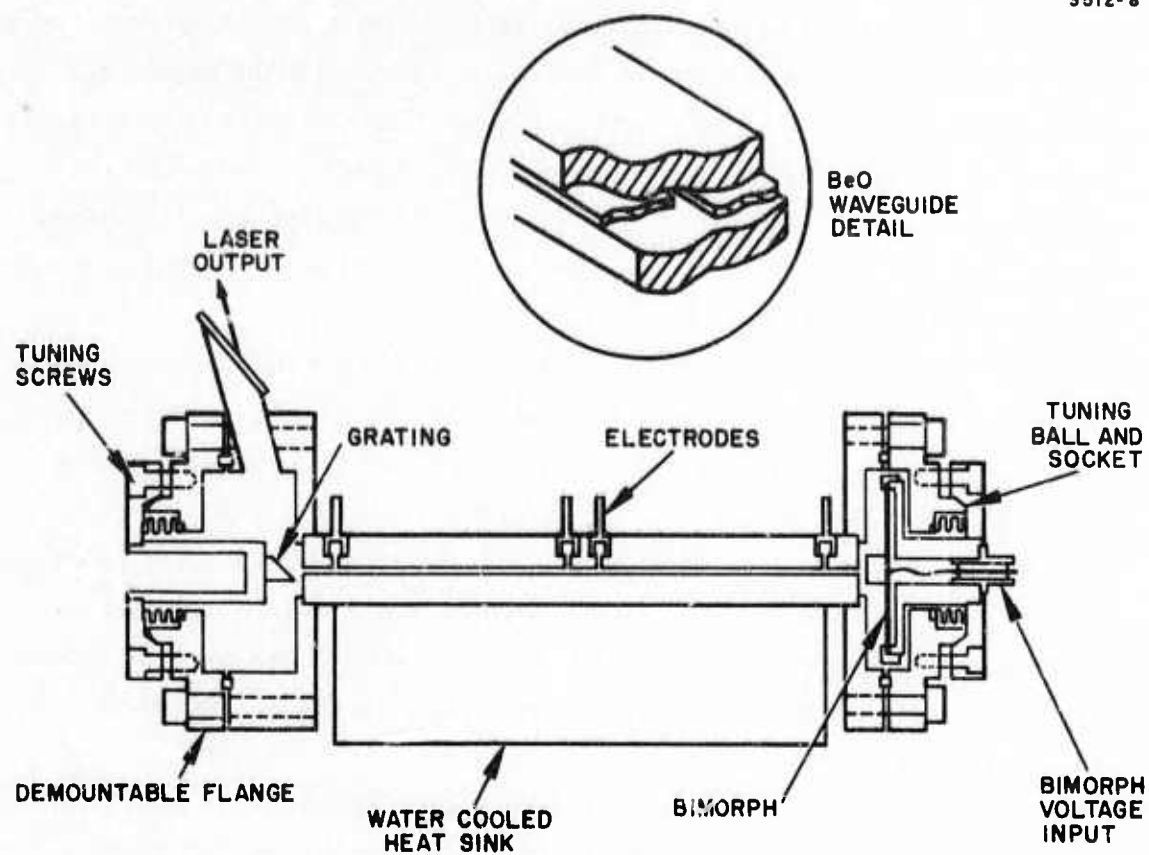


Fig. 4. Adjustment device mounted on a square bored tube.

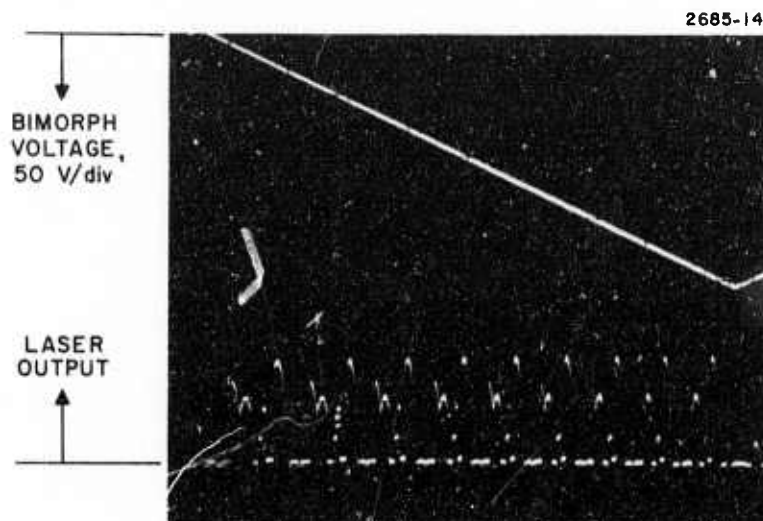


Fig. 5. Laser output and bimorph voltage.

The electrodes consist of hollow nickel pins epoxied into the countersunk holes. The 1.5-mm circular bore laser is mounted into an aluminum heat sink as shown in the photograph in Fig. 6(a). Evacuation and gas fill are provided by the feedthrough in one of the flanges as shown. The aluminum heat sink is cooled by flowing tap water. The 1.0-mm square bore laser is shown mounted on its heat sink in Fig. 6(b).

The laser and related hardware form a rugged and stable package. This concept of a single, monolithic structure with internally mounted mirrors should result in excellent laser frequency stability.

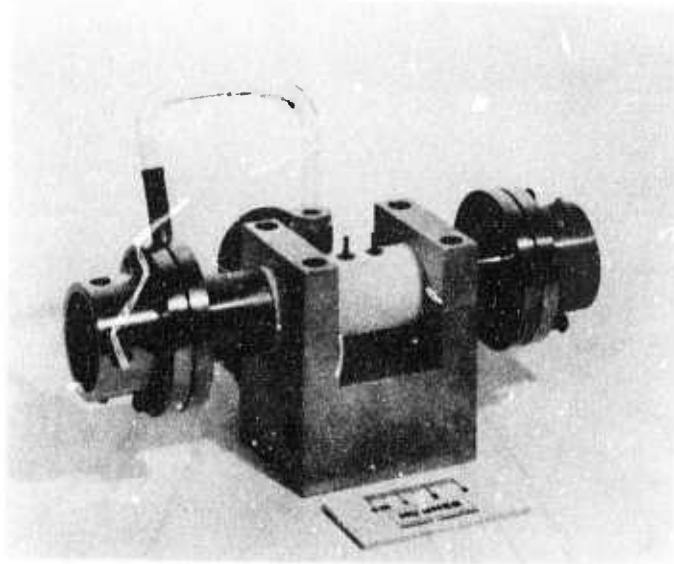
C. Power Measurements

During the course of this program, each tube was tested for power output with a 96% reflecting, 3% output coupler mirror. The other mirror was a 99% protected silver reflector. Both mirrors were flat and placed within 1 mm of the end of the waveguide.

Two 1.5 mm x 9.5 mm circular bore tubes were built for this program, and have been designated A-17 and A-18. Output power measurements for these tubes showed an optimum pressure of 140 Torr for a $\text{He}:\text{CO}_2:\text{N}_2:\text{Xe}$ mixture of 4:1:0.5:0.25. Tube A-18 produced 1.1 W while A-17 gave only 0.9 W. All subsequent data on 1.5-mm circular tubes will be for A-18. Later measurements in our inspection shop showed that A-18 had a straighter bore. Bore straightness is an important quality in determining waveguide loss, as discussed later in this report.

Two square tubes, A-20 and A-22, were tested for output power. They have 1.0 mm and 0.75 mm square cross sections, respectively. The output power versus total gas pressure for various gas mixtures is shown in Figs. 7 and 8. Note that the output powers are comparable and both lasers operate in roughly the same pressure range. There appears to be no advantage to the 0.75-mm tube, so no attempt was made to test 0.50-mm tubes. It does appear that for dimensions as small as 0.75 mm, the waveguide losses for polished

M9864



(a)

M10137

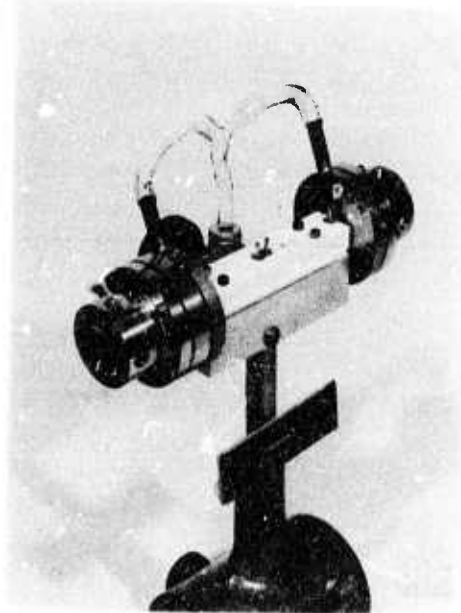


Fig. 6. Tunable laser with (a) i.d. circular bore and (b) 1.0 mm square bore.

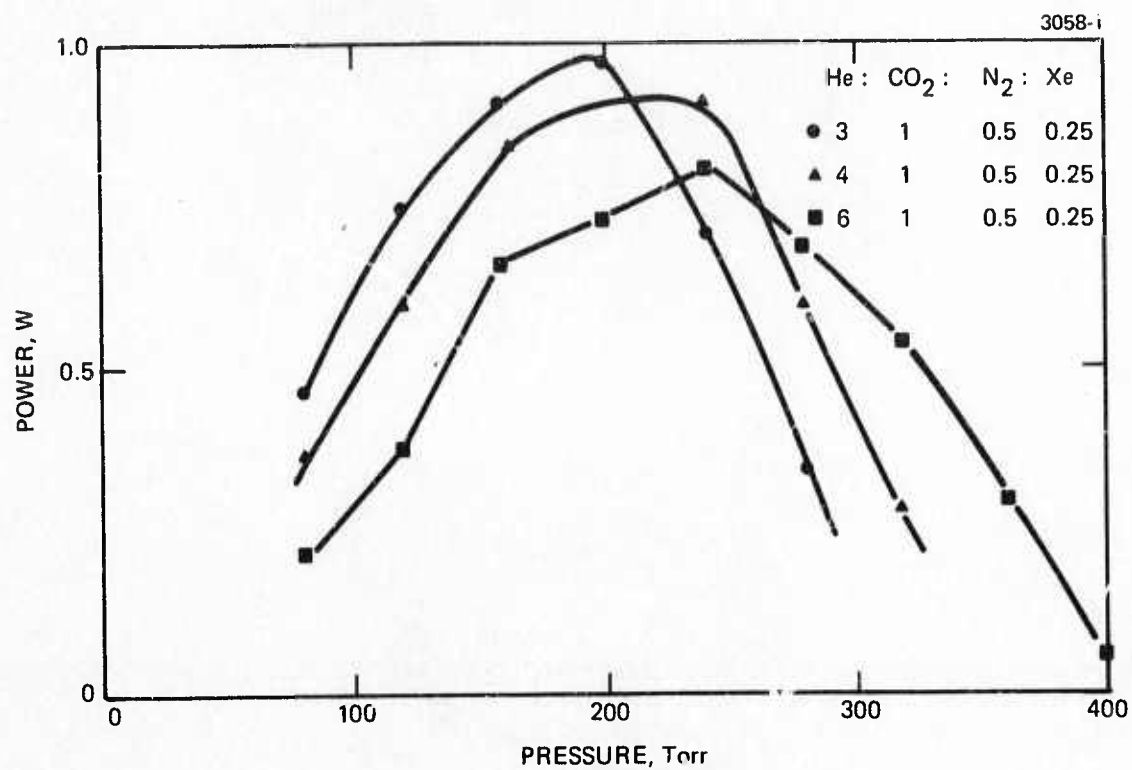


Fig. 7. Output power versus gas pressure for tube A-20.

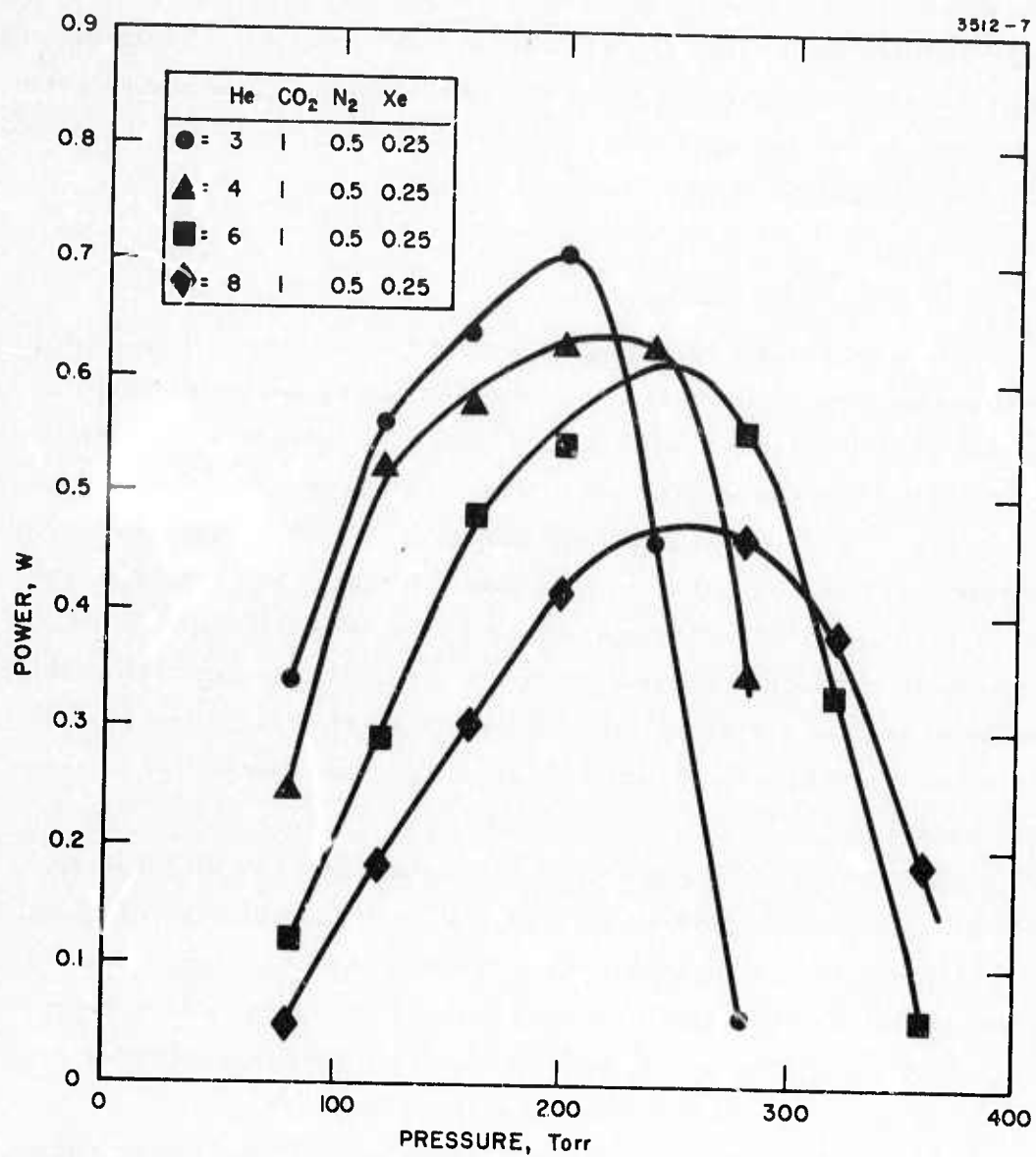


Fig. 8. Output power versus gas pressure for tube A-22.

BeO, plates are tolerable. However, as will be seen in this section, the tuning range for this size tube is not satisfactory. It is significant, however, that the available power from 1.0 mm and 0.75 mm tubes is about the same as obtained from 1.5-mm circular bore tubes of the same length, but the optimum pressure is in the 200 to 300 Torr region, where the linewidth is greater than 1 GHz.

D. Tuning Experiments

Measurements of tuning range for these lasers have been made by observing the signature of the laser output as a linear ramp voltage is applied to the bender bimorph. This also provides a convenient technique for testing the bender bimorphs. The experimental arrangement for tuning range measurements is shown in Fig. 9. The output of the tunable laser is monitored with a monochromator and detected with a dc-coupled photoconductor. A linear ramp voltage generator drives the bender bimorph. The output of the laser versus bimorph voltage can be displayed either on an oscilloscope (fast scan) or on an X-Y recorder (slow scan). Both techniques have been employed in these experiments.

The bender bimorphs have the capability of scanning over several half-wavelengths at $10.6\text{ }\mu\text{m}$, allowing the display of a number of free spectral ranges in the laser tuning characteristic. One free spectral range corresponds to 1530 MHz of tuning for our 9.8-cm laser cavities. This serves as a calibration for measuring the frequency range over which a single line may be tuned.

Measurements of the laser signature, and thus tuning range, were made under a variety of conditions for each of the tubes. For tube A-18, the largest tuning range, when power was extracted from the 96% reflecting output coupler, occurred at a pressure of 140 Torr with a $\text{He}:\text{CO}_2:\text{N}_2:\text{Xe}$ mixture of 4:1:0.5:0.25. Under these conditions, tube voltage and current were 4.1 kV and 2.0 mA through each side. The laser signature for this case is shown in Fig. 10. The peak laser output power is 0.65 W and the laser tuning range is 776 MHz. The tuning range over which the power level exceeds half the peak value

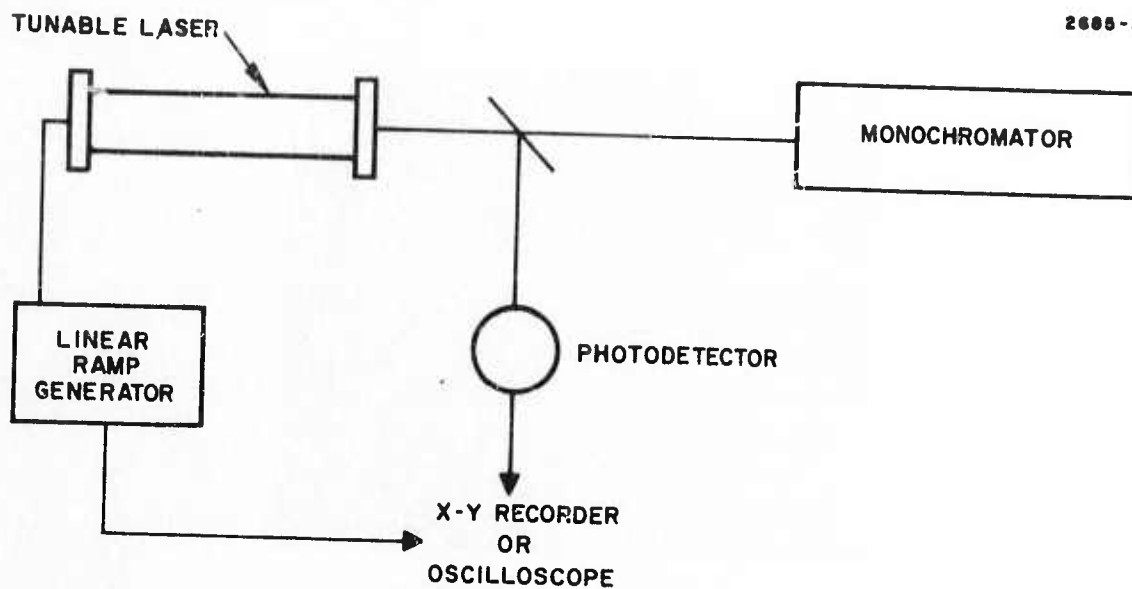


Fig. 9. Experimental arrangement for tuning range measurements.

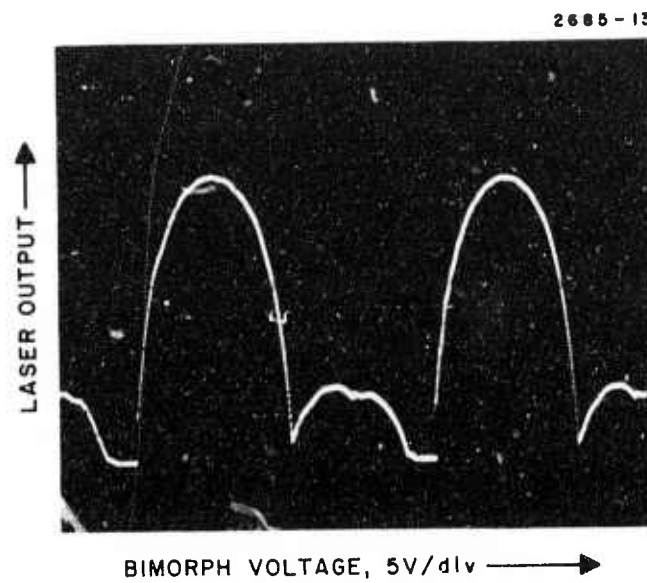


Fig. 10.
laser output power versus bimorph
tuning for tube A-18. Power is
extracted from 98% R output
coupler.

(3 dB tuning range) is 674 MHz. Note that three lines lase over different parts of the laser tuning curve, but the highest power transition, P(20), is lasing alone over its tuning curve. This fact was confirmed by observation with the monochromator.

Tube A-20 (1.0 mm square) was fitted with a diffraction grating and 96% R output mirror. Tuning curves were obtained in the same manner as for A-18. Representative data are shown in Fig. 11 for an 8:1:0.5:0.25 mixture of He:CO₂:N₂:Xe. The maximum tuning range observed here is ~930 MHz. The tuning range and output power are plotted versus pressure in Fig. 12 for different gas mixtures. It is seen that the maximum tuning range and maximum power both occur at approximately the same pressure (~200 Torr for this mixture), as predicted by the theory of Degnan.⁴ The maximum output power is ~0.5 W.

The output mirror was then replaced with a total reflector and the output power is coupled off of the zeroth order of the grating. This coupling was rather small, resulting in only 80 mW of laser power at the P(20) line center, but allowing us to measure the tuning range. Representative data for the 8:1:0.5:0.25 mixture are shown in Fig. 13. The maximum tuning range was observed to be 1200 MHz at a total pressure of 260 Torr. The tube voltage and current are 6.6 kV and 1.5 mA through each side. We have found that the tuning range increases for lower tube current, probably due to decreased gas heating (higher density) and higher gain, even though laser output power is lower at lower current.

Tube A-22 (0.75 mm square) was fitted with identical optics as A-20. Tuning curves were obtained and are shown in Fig. 14 for an 8:1:0.5:0.25 mixture of He:CO₂:N₂:Xe. Maximum tuning occurs at a pressure of 280 Torr, and is 840 MHz, much less than was obtained from tube A-20. It is believed that the reduced tuning is due to a decrease in grating efficiency when operating on such a small area. Only ~110 lines of the grating are illuminated for a 0.75 mm spot. The power output at line center is 50 mW, also less than observed for the 1.0-mm square tube.

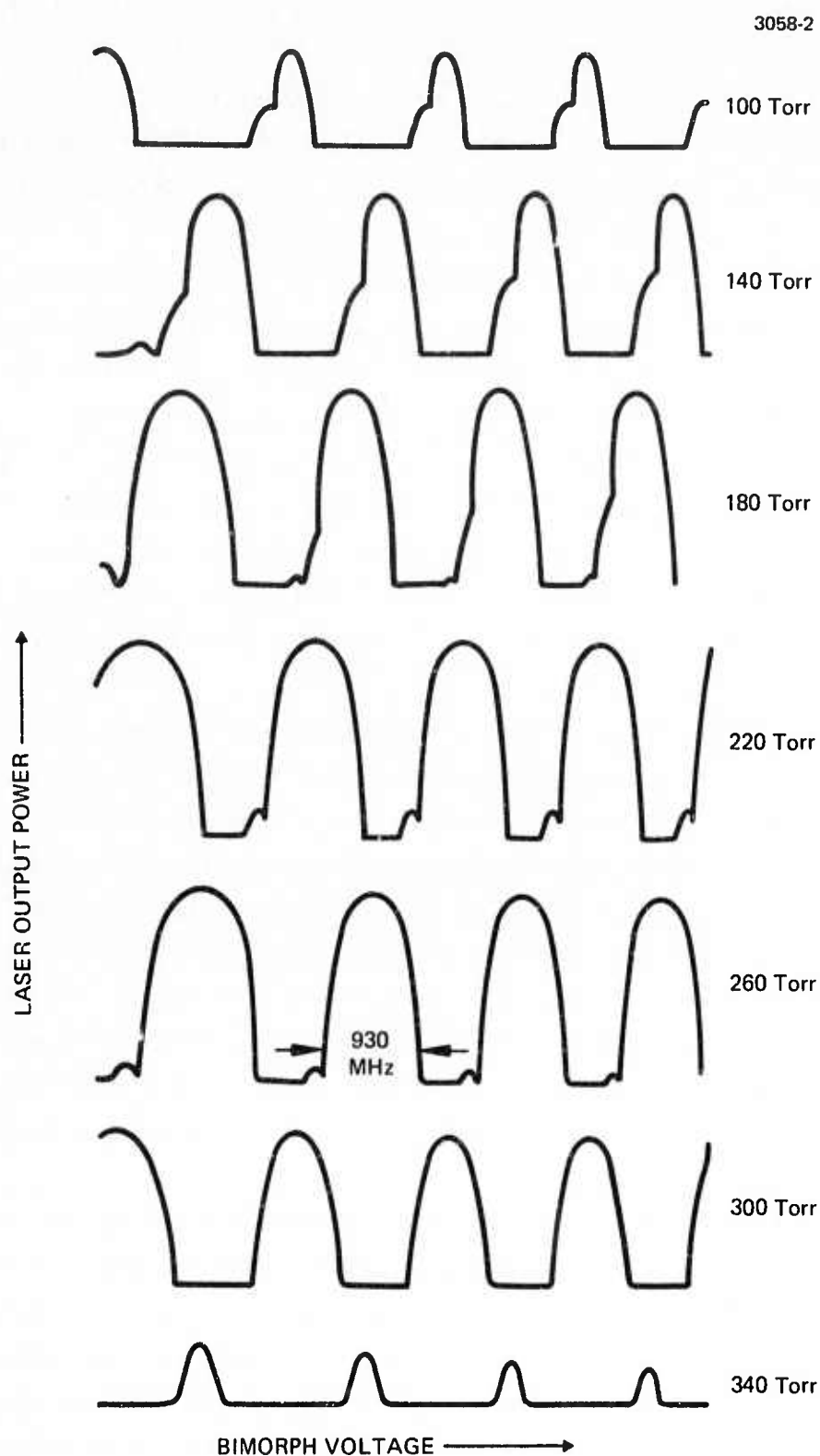


Fig. 11. Tuning characteristic of tube A-20, with power taken through output mirror, for various total gas pressures.

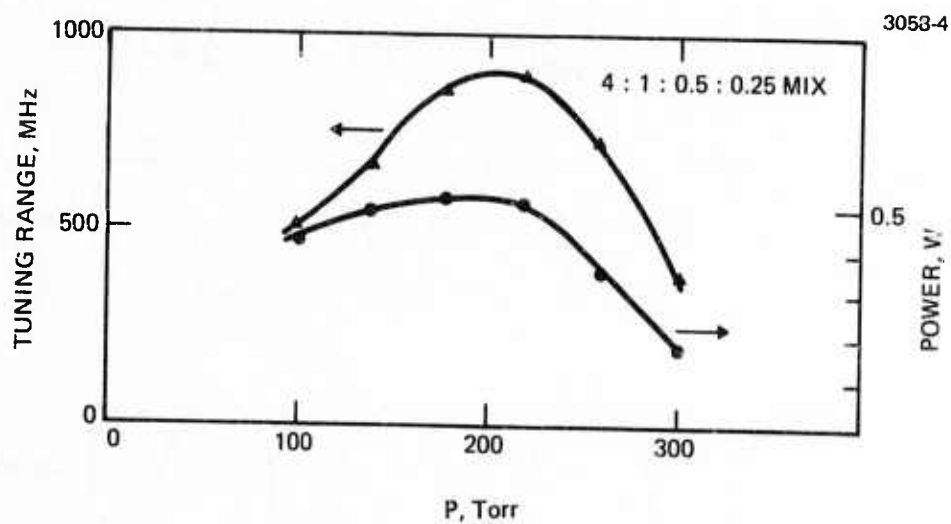
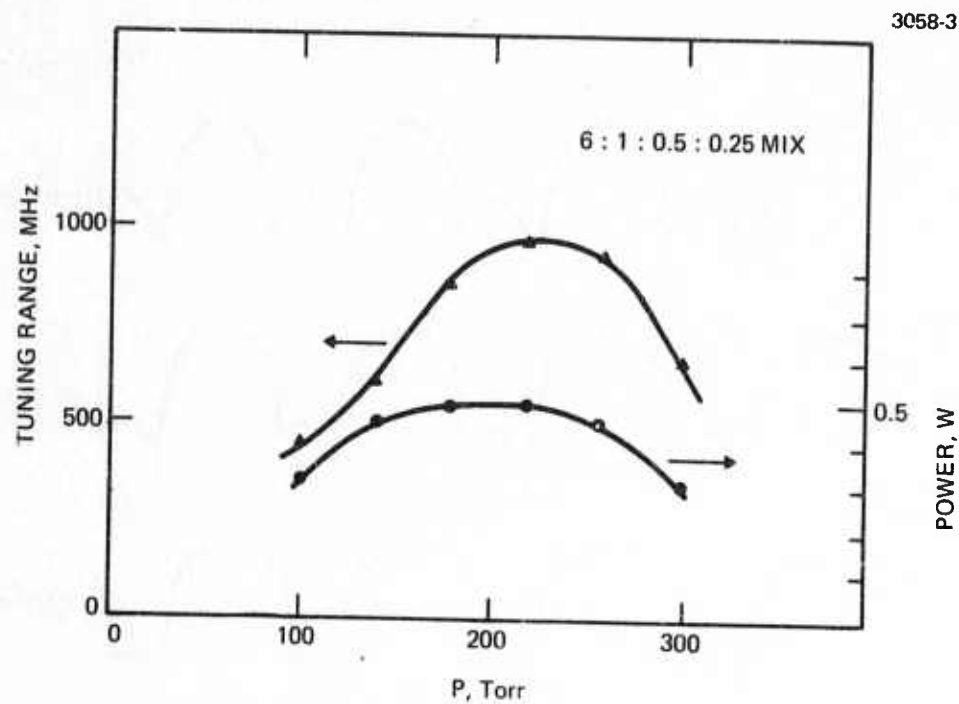


Fig. 12. Observed tuning range and output power versus pressure for tube A-20, with power extracted from 96% R output coupler.

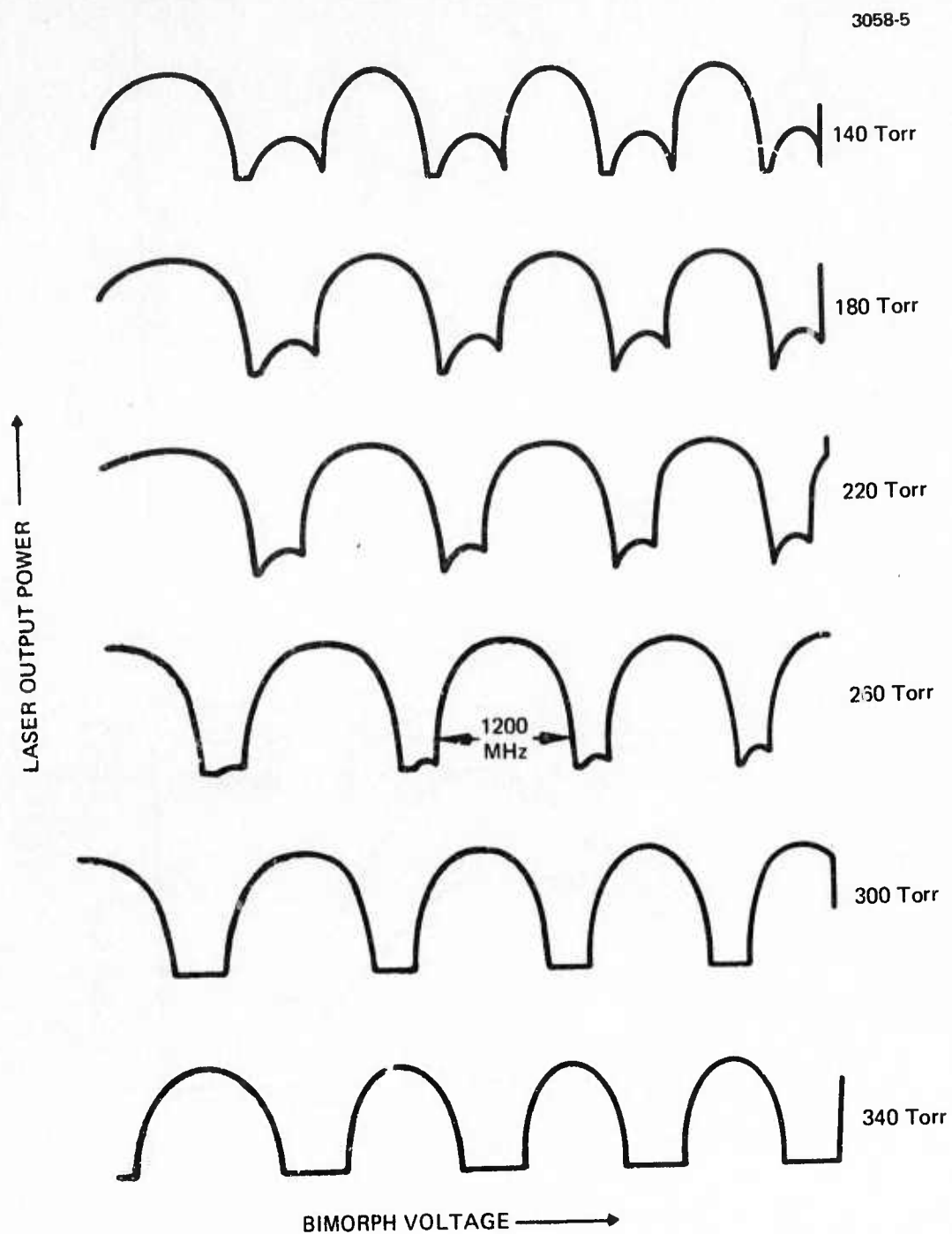


Fig. 13. Tuning characteristic of tube A-20, with power coupled off of grating, for various total gas pressures.

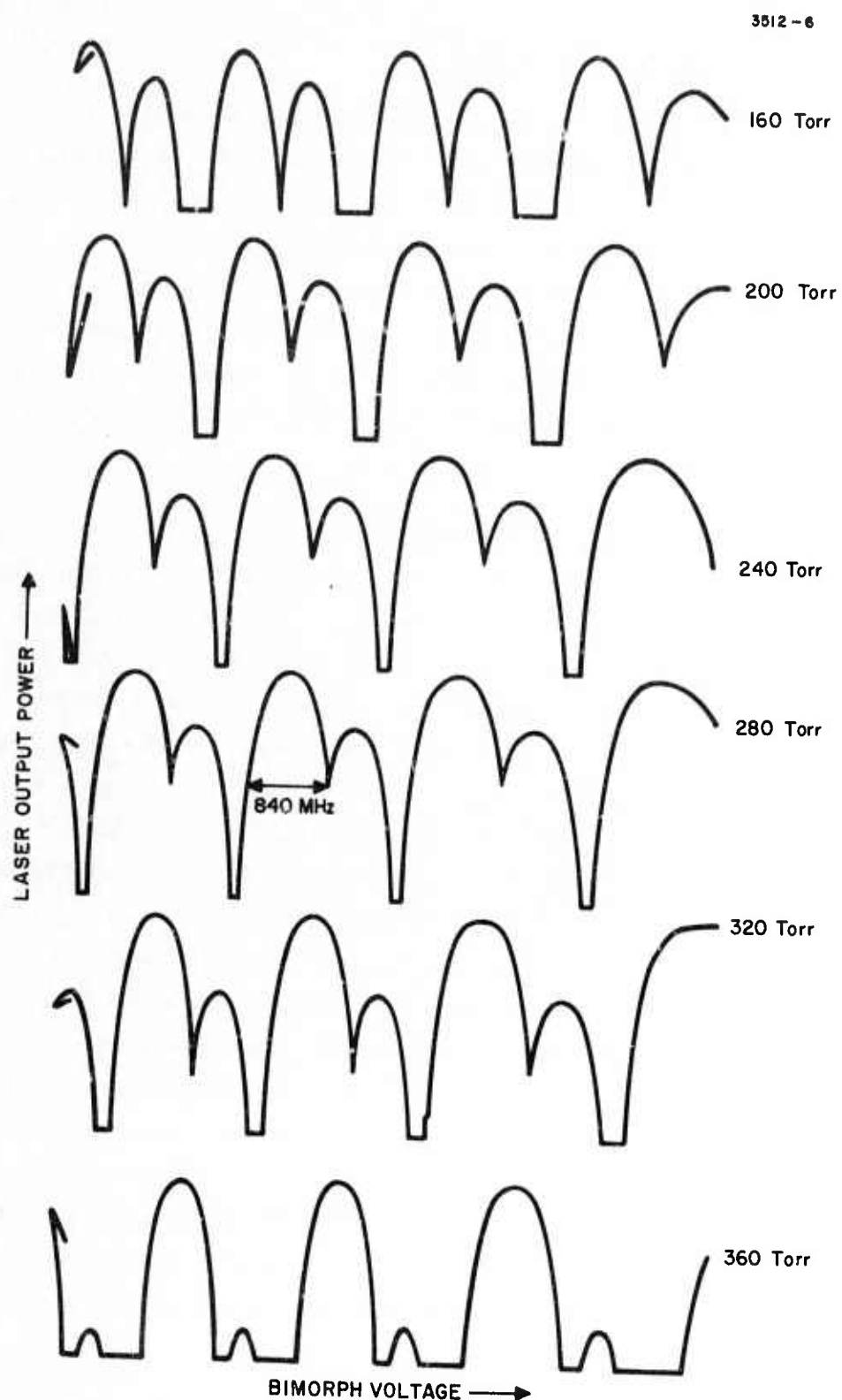


Fig. 14. Tuning characteristic of tube A-22, with power coupled off of grating for various total gas pressures.

E. Final Design and Performance

One of the contractual requirements of this program is to deliver a tunable waveguide laser to a laboratory to be designated by the contract officer. In this section we describe the design and demonstrate the performance characteristics of this device.

It is clear from the data of the previous sections that the best performance has been obtained from A-20, the 1.0-mm square waveguide laser. A new tube (A-23), with a 40 cm³ ballast volume, refill valve, and heat sink mount has been constructed. A photograph of this tube is shown in Fig. 15.

1. Operating Characteristics

The optimum operating pressure for this tube was found to be in the 240 to 260 Torr region, using an 8:1:0.5:0.25 mixture of He:CO₂:N₂:Xe. In Fig. 16, we show the tuning curve for a 260 Torr gas fill, where the power is coupled off the grating (zero order). The laser tuning range is ~1150 MHz. Approximately 32 V are required to tune one free spectral range at 10.6 μ m. The laser operates on P(20) at 10.6 μ m and the line center output power is ~90 mW.

The power supply voltage and current for this tube is 8.34 kV and 3.0 mA, where 1.5 mA passes through each section and a 2 M Ω ballast resistor. The tube voltage is 5.34 kV. A pulse starting circuit is needed to initiate the two discharge paths. The circuit used is similar to the circuit discussed in Section III (with manual operation), and is shown in Fig. 17. The ballast resistors and starting circuit will be delivered with the tube. In order to start the tube, the power supply voltage is raised to a point just below where the tube fires spontaneously. The pulse is then injected into the high voltage lead by pressing a switch on the starting circuit, and both sides of the tube will light. This works about half the time, usually requiring several attempts to start the laser.

M10473

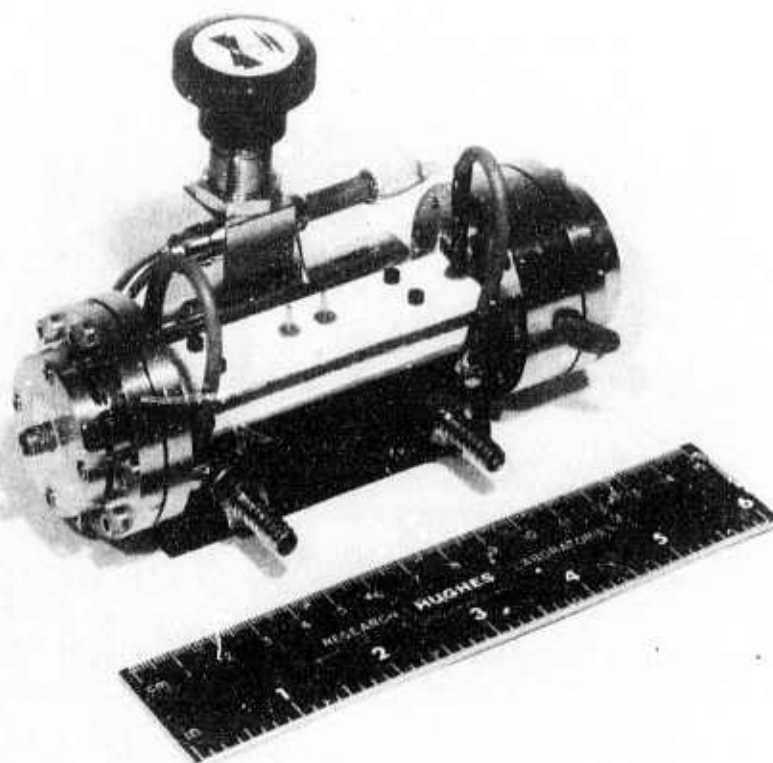


Fig. 15. 1.0 mm square waveguide laser in final form.

3512-4

3 dB TUNING RANGE = 1050 MHz

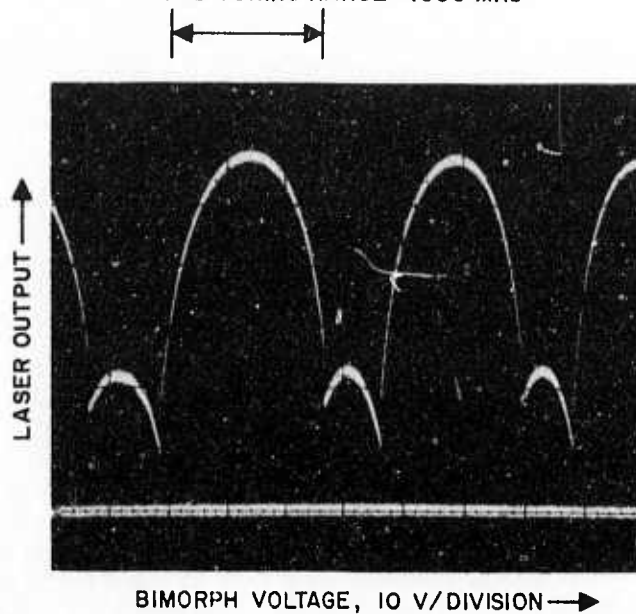


Fig. 16.
Laser output power versus bimorph
tuning for tube A-23. Power is
extracted from the grating. The
solid white line represents the
zero power level.

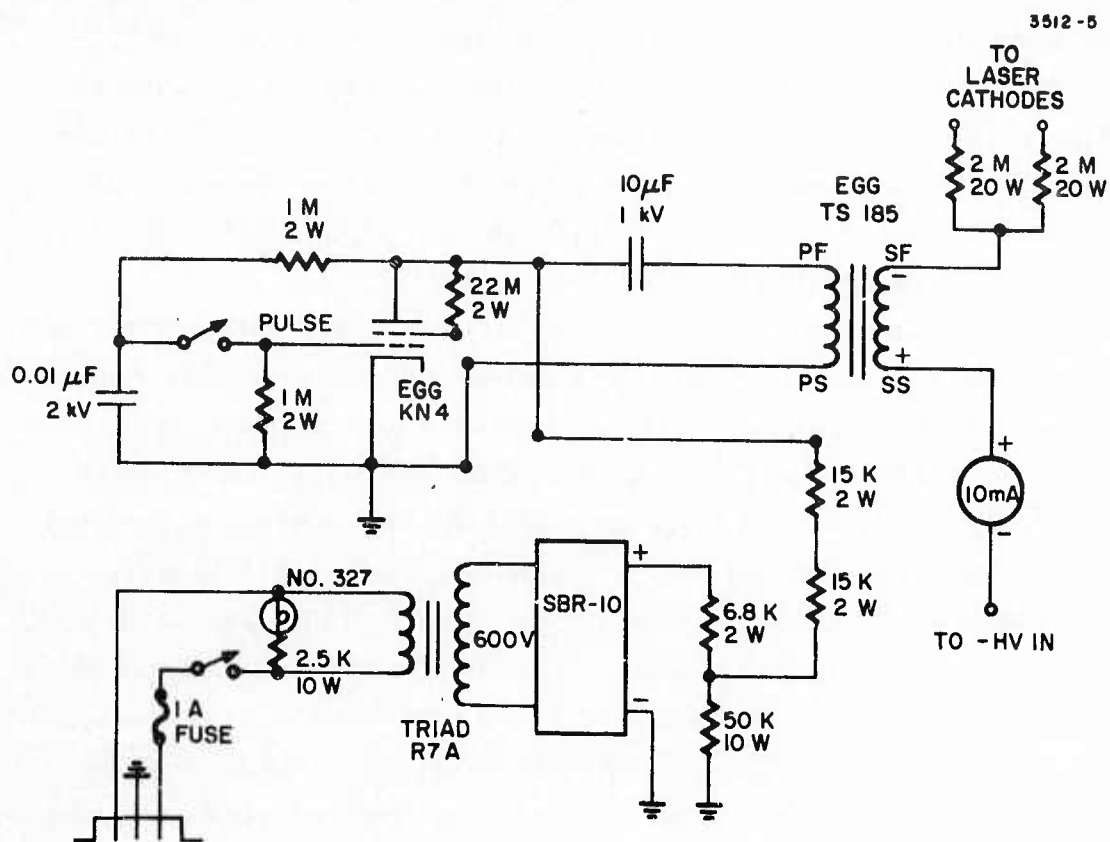


Fig. 17. Laser starting circuit.

2. Frequency Stability

Frequency stability measurements were reported for tubes A-17 and A-18 in the 19 March 1973 to 31 December 1973 Interim Technical Report for this contract. The results were not very satisfactory, primarily due to a 2.2 kHz mechanical resonance in the structure. This problem has been eliminated by a redesign of the mirror mounts and tighter clamping of the bimorph. This is evident in the increased voltage required to translate the bimorph one free spectral range (~ 32 V as opposed to ~ 25 V previously).

The frequency stability of A-23 was measured with respect to a conventional CO_2 laser mounted in a resonator built on an invar tube. Both lasers are electrically driven by 10 kV Fluke power supplies, which have a peak-to-peak ac ripple of less than 5 mV. Both tubes are conduction cooled to aluminum baseplates which are water cooled. The experimental arrangement is shown in Fig. 18. The beat frequency between the two lasers is detected in a HgCdTe photodiode and displayed on a spectrum analyzer. The spectral beat is also passed through a 30 MHz discriminator for a real time display of frequency versus time on an oscilloscope. The frequencies of the lasers are individually set by controlling the voltages on their respective bimorphs. Low noise power supplies are used for this purpose. The beat frequency can be varied up to ~ 600 MHz, but is usually set ~ 100 MHz. For use of the discriminator, of course, the beat frequency is set to 30 MHz.

The spectral beat, as observed on the spectrum analyzer, is shown in Fig. 19 for several different sweep rates. The spectral width is ~ 10 kHz in these measurements. The discriminator output is shown in Fig. 20 for a beat frequency of 30 MHz. There is a fairly wideband FM noise level with an rms value of 10 kHz, consistent with the spectrum analyzer result. There is also a train of small spikes with ~ 8 kHz peak amplitude, which occur at a 60 Hz rate.

These results show an immense improvement since the past reporting period, but still fall short of the program goal (< 1 kHz). The remaining frequency instabilities are thought to be due to acoustic

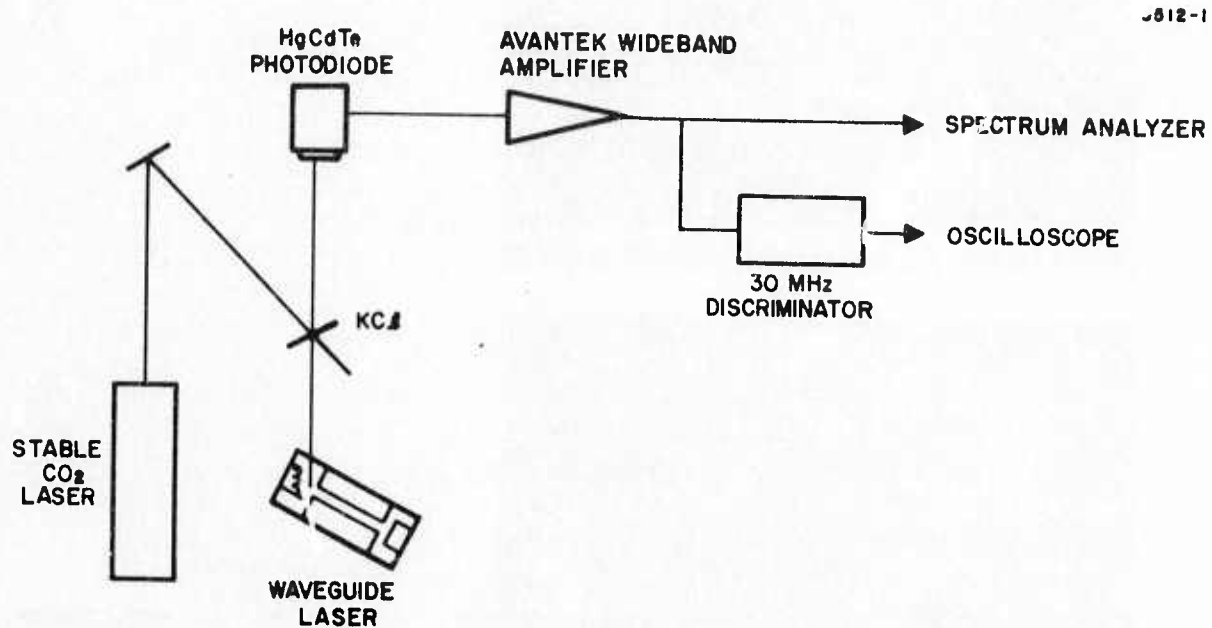


Fig. 18. Experimental arrangement for frequency stability measurements.

3512-2

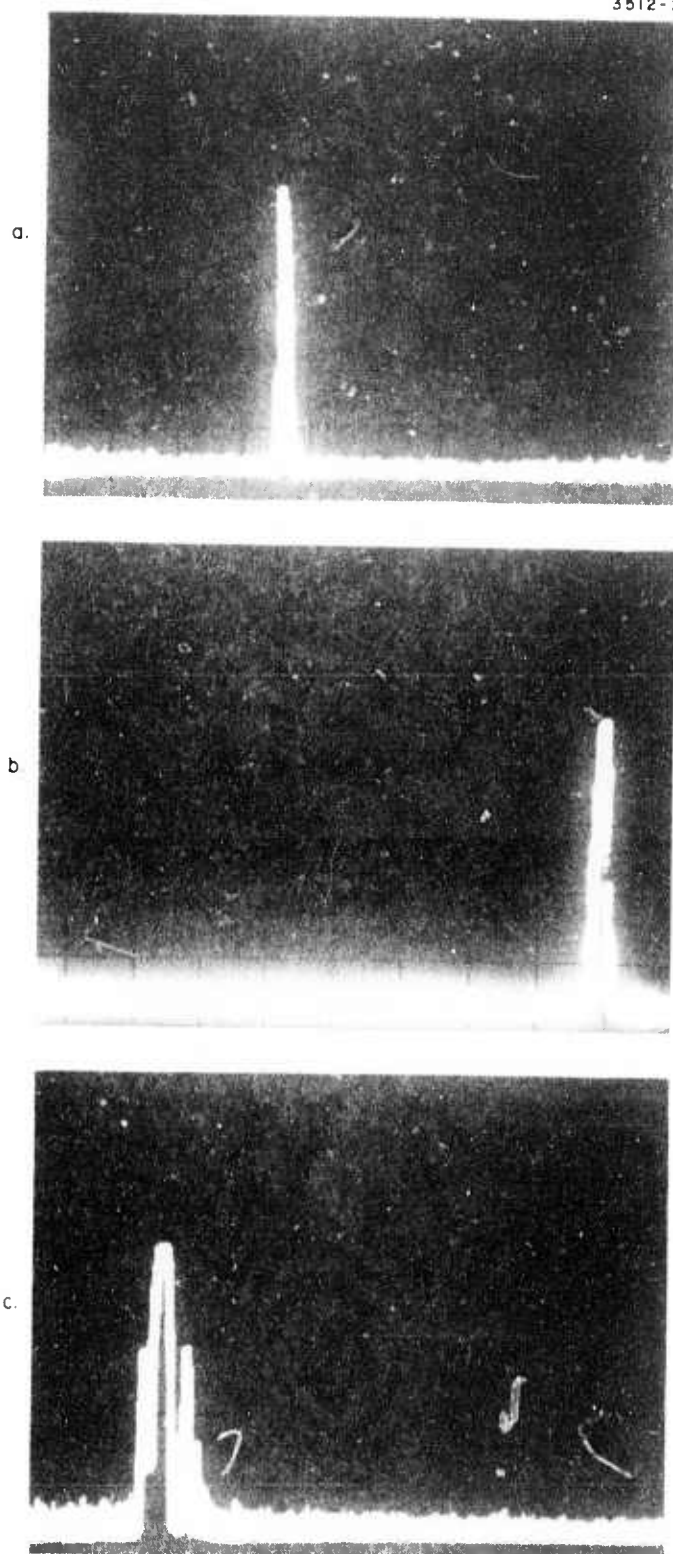


Fig. 19.
Spectrum analyzer
displays of beat fre-
quency. Horizontal
scale is (a) 100 kHz/
div, (b) 50 kHz, and
(c) 20 kHz/div, with
a sweep speed of 10 ms/
div. The IF bandwidth
is 3 kHz and vertical
scale is 10 dB/div.
Center frequency is
65 MHz.

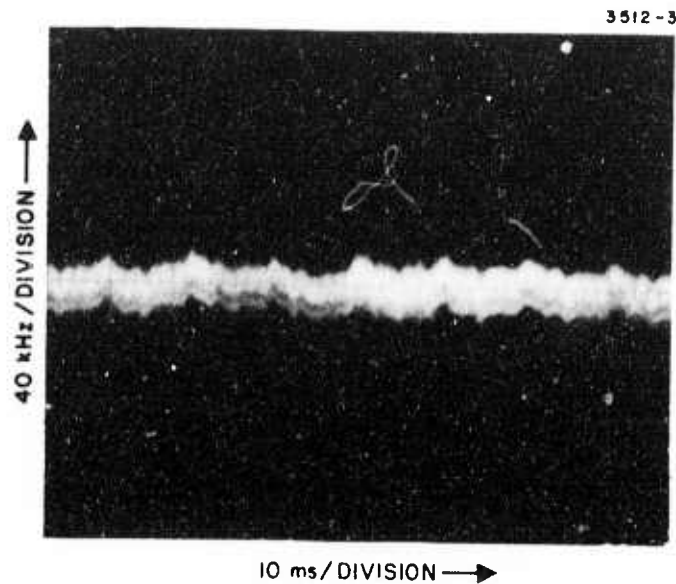


Fig. 20.
Output of frequency discriminator
when beat frequency is set at 30 MHz.

pickup in the room and noise from the water flow in the heat sinks. Also, it is not known which laser contributes the largest frequency instability. It is hoped that by repeating the experiment in a more quiet acoustic environment and by mixing the waveguide laser with a very stable laser of the type used at Lincoln Laboratory, the program goal will be met.

III. WAVEGUIDE POWER AMPLIFIER

A. Summary

The goal of this task is the analytical and experimental study of CO₂ waveguide laser amplifiers for laser radar applications. These studies are then utilized to develop a physical design for a proposed device. In part B, we review the amplifier analysis. Parts C through E describe the construction considerations and measurements on a 1-m test bed, and part F includes the discussion and the presentation of a physical design for a full scale device.

B. Waveguide Amplifier Theory

1. Basic Equations

In this section we will derive expressions relating independent amplifier parameters such as overall length, small signal gain coefficient, and linewidth to system design requirements such as overall gain, output power, and output linewidth. The solutions will include the effects of distributed loss as well as gain saturation. The results are most easily displayed in the form of design curves, which will be presented for the case of negligible distributed loss. The application of the theory to a double-pass configuration also will be considered.

The frequency-dependent saturation of small signal gain is described by

$$a(\nu) = \frac{a_o}{\left[1 + \frac{I(\nu)}{I_s(\nu)}\right] [1 + \delta^2]} \quad (1)$$

In this equation, $a(\nu)$ is the saturated gain at frequency ν , a_o is the small signal gain at line center, $I(\nu)$ and $I_s(\nu)$ are the beam intensity and saturation intensity at frequency ν , and δ is the normalized frequency detuning given by

$$\delta = \frac{2(\nu - \nu_o)}{\Delta\nu} , \quad (2)$$

where $\Delta\nu$ is the unsaturated gain linewidth and ν_o is the line center frequency. The saturation intensity $I_s(\nu)$ may be related to the saturation intensity at line center by

$$I_s(\nu) = (1 + \delta^2) I_s(\nu_o) . \quad (3)$$

Substituting this expression into eq. (1) and writing $\gamma(\nu) = I(\nu)/I_s(\nu_o)$, we obtain

$$a(\nu) = \frac{a_o}{1 + \delta^2 + \gamma} . \quad (4)$$

The incremental gain may be written as

$$\frac{1}{I(\nu)} \frac{dI(\nu)}{dZ} = a(\nu) - \beta , \quad (5)$$

where β is the distributed loss. This relationship may be rewritten as

$$\frac{1}{\gamma} \frac{d\gamma}{dZ} = \frac{a_o}{1 + \delta^2 + \gamma} - \beta . \quad (6)$$

The above equation may be solved directly by separation of variables. The solution is

$$\frac{a_o L}{1 + \delta^2} - \beta L = \ln \frac{\gamma_2}{\gamma_1} - \frac{a_o}{\beta(1 + \delta^2)} \ln \frac{a_o - \beta(1 + \delta^2) - \beta\gamma_2}{a_o - \beta(1 + \delta^2) - \beta\gamma_1} , \quad (7)$$

where γ_1 is the normalized input intensity (assumed constant with frequency), $\gamma_2(\nu)$ is the normalized output intensity, and L is the amplifier length.

For a given set of required amplifier conditions, eq. (7) may be used to study design tradeoffs in small signal gain, linewidth, and overall length. Such an analysis has shown that for the device under consideration ($a_o > 10\beta$), the distributed loss may be neglected in the

amplifier equations with very little loss in accuracy. We will then proceed by assuming $\beta \ll \alpha_o$. In this case, eq. (7) reduces to

$$\alpha_o L = (1 + \delta^2) \ln \frac{\gamma_2}{\gamma_1} + (\gamma_2 - \gamma_1) \quad (8)$$

For large gains we may assume $\gamma_1 \ll \gamma_2$, and write

$$\gamma_2(\nu) = \alpha_o L - (1 + \delta^2) \ln \frac{\gamma_2(\nu)}{\gamma_1} \quad (9)$$

At line center ($\delta = 0$) eq. (9) becomes

$$\gamma_2(\nu_o) = \alpha_o L - \ln \frac{\gamma_2(\nu_o)}{\gamma_1} \quad (10)$$

The last term in eq. (10) is related to G , the saturated gain (at line center) in dB, by

$$G = 4.34 \ln \frac{\gamma_2(\nu_o)}{\gamma_1} \quad (11)$$

Substituting eqs. (10) and (11) into eq. (9) and solving for δ , we obtain

$$\delta = \frac{2(\nu - \nu_o)}{\Delta\nu} = \left(\frac{\gamma_2(\nu_o) - \gamma_2(\nu) - \ln \frac{\gamma_2(\nu)}{\gamma_2(\nu_o)}}{\ln \frac{\gamma_2(\nu)}{\gamma_2(\nu_o)} + 0.23 G} \right)^{1/2} \quad (12)$$

Equation (12) may be used to obtain the frequency dependence of $\gamma_2(\nu)$ for various values of the system gain G and the output intensity at line center $\gamma_2(\nu_o)$. The variation of the half-power line width $\Delta\nu_{3 \text{ dB}}$ of $\gamma_2(\nu)$ may be obtained (for large gain) from eq. (12) using $\gamma_2(\nu) = 1/2 \gamma_2(\nu_o)$. Thus we obtain

$$\Delta \nu_{3 \text{ dB}} = \Delta \nu \left(\frac{\gamma_2(\nu_o)/2 + \ln 2}{0.23 G - \ln 2} \right)^{1/2} \quad (13)$$

The effects of gain saturation on the output linewidth are clearly evident in eq. (13). At low levels of saturation ($\gamma_2(\nu_o) \ll 1$), the output linewidth is reduced (gain narrowing) by a factor approximately proportional to $G^{-1/2}$, or $(a_o L)^{-1/2}$. As saturation becomes important, the output is broadened again (power broadening), and the linewidth may even exceed the small signal gain linewidth $\Delta \nu$. This variation is displayed in Fig. 21, which is a plot of the normalized output linewidth as a function of the normalized line center intensity for various values of the overall gain; this figure contains all the amplifier information that is required for a practical device design. In Fig. 22 we have also plotted complete line profiles for several typical sets of amplifier parameters (using eq. (12)). Power broadening is effective throughout the line profile. This is not true when distributed loss is present; in this case, the line is truncated at the frequencies where the unsaturated gain equals the distributed loss.

2. Double-Pass Amplifier

The extension of the above approach to a double-pass configuration is straightforward. We consider the experimental arrangement shown in Fig. 23. The intensities in the $+$ and $-$ directions are now labeled $I_+(\nu)$ and $I_-(\nu)$, respectively. The gain saturation equation may now be written as

$$a(\nu) = \frac{a_o}{1 + \delta^2 + \frac{I_+(\nu) + I_-(\nu)}{I_s(\nu_o)}} \quad (14)$$

By definition, the incremental gain may also be written as

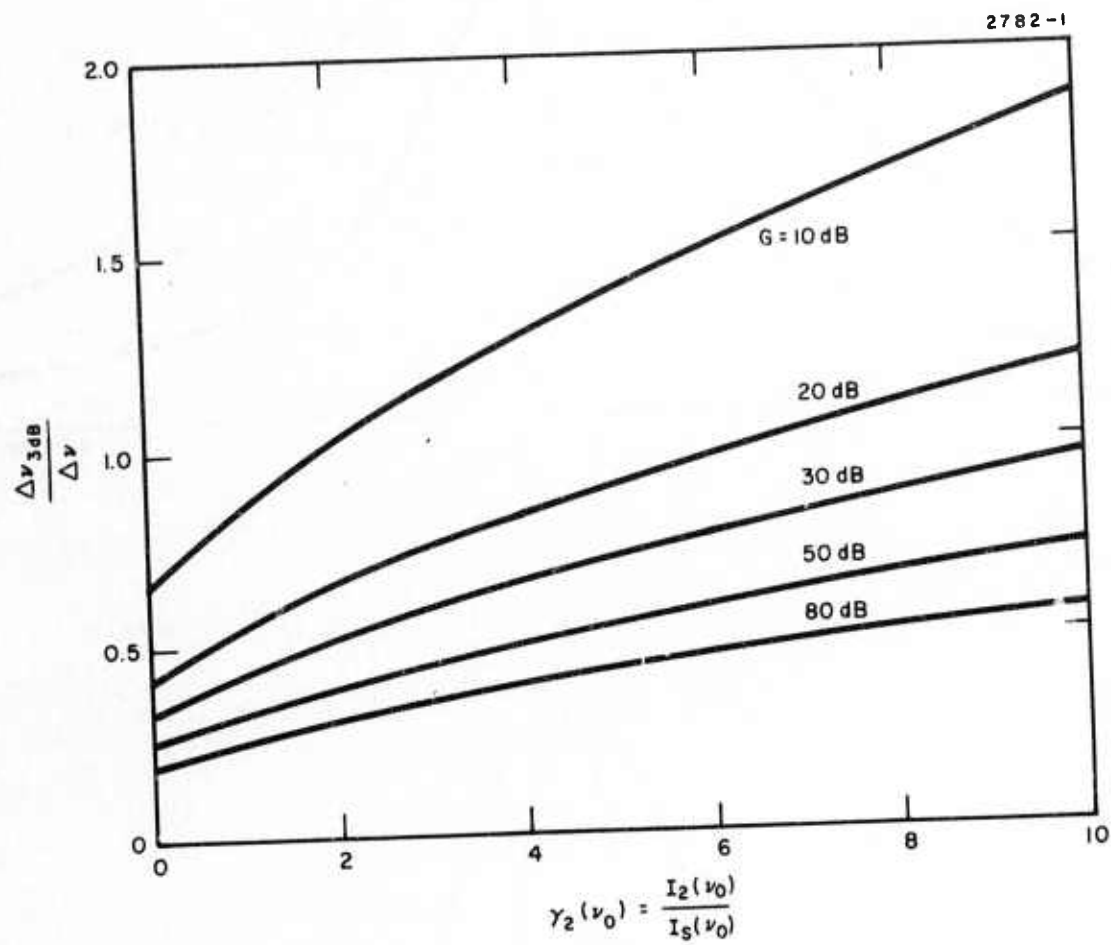
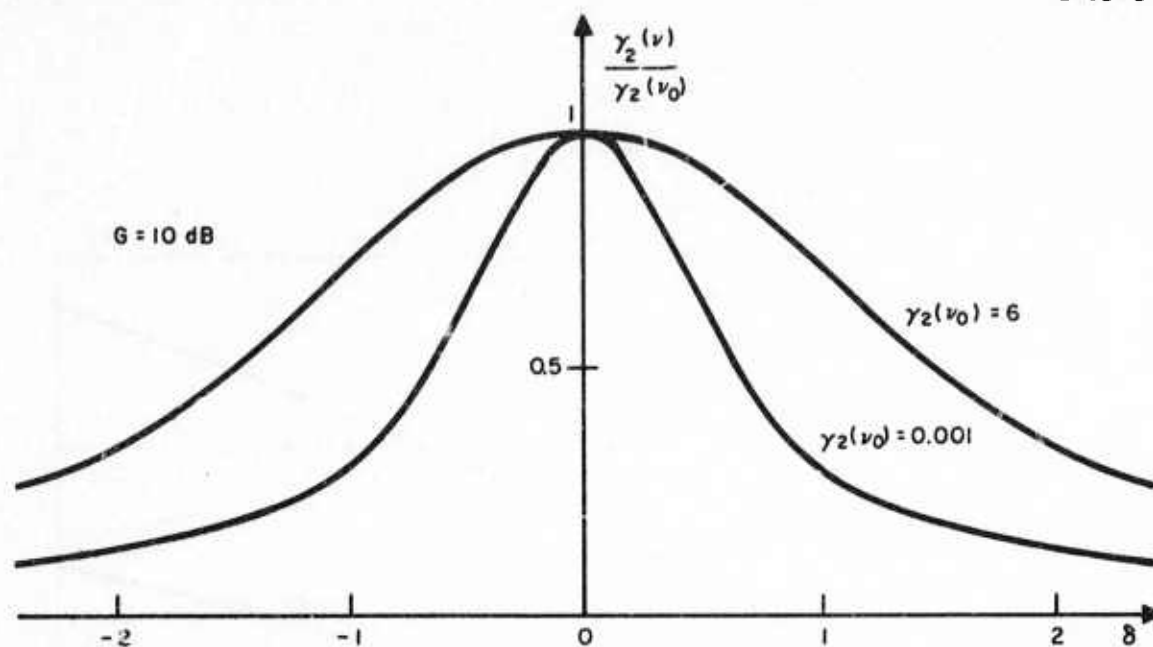


Fig. 21. Normalized output linewidth versus normalized output intensity for several values of overall gain.

2782-2



2782-3

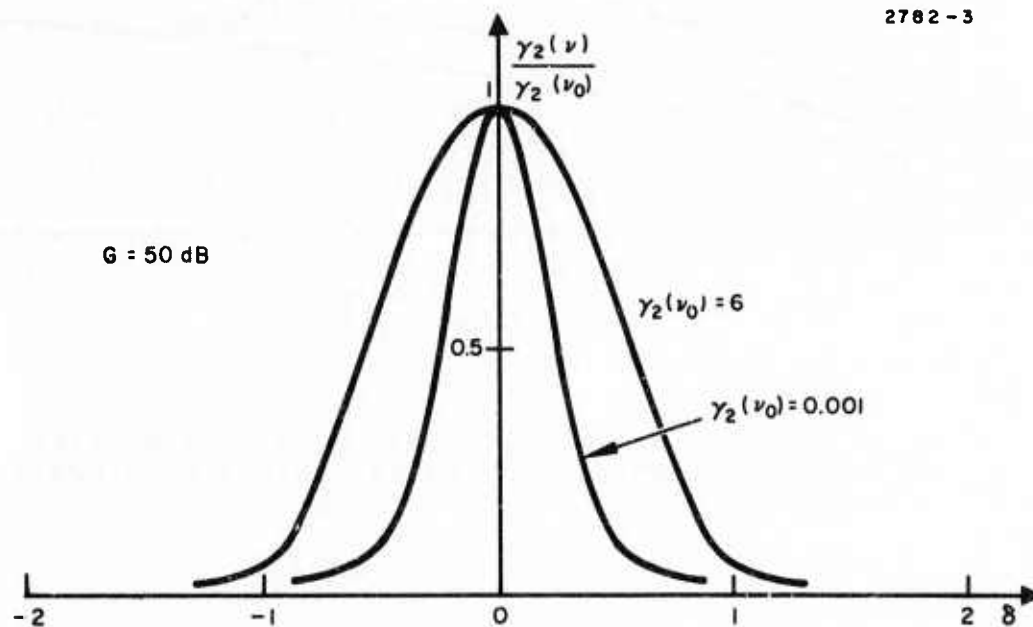


Fig. 22. Normalized line profiles for $G = 10$ dB (upper) and $G = 50$ dB (lower).

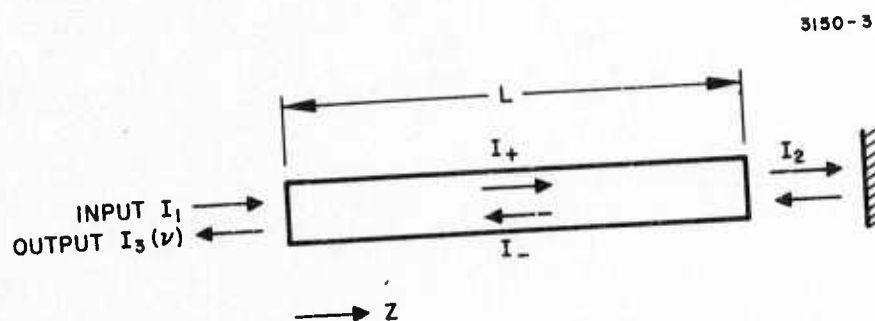


Fig. 23. Double-pass amplifier configuration.

$$a(\nu) = \frac{1}{I_+} \frac{dI_+}{dZ} \quad (15)$$

$$a(\nu) = \frac{1}{I_-} \frac{dI_-}{dZ} \quad (16)$$

If we now substitute $\gamma_+(\nu) = I_+(\nu)/I_s(\nu_0)$ and $\gamma_-(\nu) = I_-(\nu)/I_s(\nu_0)$ into eqs. (15) and (16) and then combine the two equations, we obtain

$$\frac{d\gamma_+}{\gamma_+} = - \frac{d\gamma_-}{\gamma_-} \quad (17)$$

The solution to this equation is

$$\gamma_+ \gamma_- = C, \quad (18)$$

where C is a constant. Combining eqs. (14), (15), and (18), we obtain

$$\frac{1}{\gamma_+} \frac{d\gamma_+}{dZ} = \frac{a_0}{1 + \delta^2 + \gamma_+ + \frac{C}{\gamma_+}} \quad (19)$$

By separation of variables and integration from 0 to L, we obtain

$$(1 + \delta^2) \ln \frac{\gamma_2}{\gamma_1} + (\gamma_2 - \gamma_1) + \frac{C}{\gamma_1} - \frac{C}{\gamma_2} = a_0 L \quad (20)$$

To eliminate γ_2 , we make use of eq. (18), applied at each end of the amplifier:

$$\gamma_1 \gamma_3 = \gamma_2^2 = C \quad (21)$$

By combining eqs. (20) and (21) we obtain

$$(1 + \delta^2) \ln \frac{\gamma_3}{\gamma_1} + 2(\gamma_3 - \gamma_1) = 2 a_0 L \quad (22)$$

By comparison, a single pass through the length L yields the relation (see eq. (8))

$$(1 + \delta^2) \ln \frac{\gamma_3}{\gamma_1} + (\gamma_3 - \gamma_1) = \alpha_o L \quad (23)$$

A more convenient comparison between the single-pass and double-pass configurations may be obtained (using the above equations) by writing expressions for the device length required to produce a given line center output $\gamma_3(\nu_o)$ and saturated gain G , for a given incremental gain α_o (we also assume $\gamma_3 \gg \gamma_1$).

$$\text{Single Pass: } L = \frac{1}{\alpha_o} [\gamma_3(\nu_o) + 0.23 G] \quad (24)$$

$$\text{Double Pass: } L = \frac{1}{\alpha_o} \left[\gamma_3(\nu_o) + \frac{0.23 G}{2} \right] \quad (25)$$

Thus the potential length decrease in going to a double-pass configuration (assuming 100% reflectivity at the end mirror) can be as much as 50%, depending on the relative magnitudes of $\gamma_3(\nu_o)$ and G .

Another parameter of interest is the half-power bandwidth; this may be obtained from eq. (22) by setting $\gamma_3(\nu) = \gamma_3(\nu_o)/2$ with the result

$$\Delta\nu_{3 \text{ dB}} = \Delta\nu \left(\frac{\gamma_3(\nu_o) + \ln 2}{0.23 G - \ln 2} \right)^{1/2} \quad (26)$$

By comparison, a single pass through the same amplifier yields

$$\Delta\nu_{3 \text{ dB}} = \Delta\nu \left(\frac{\gamma_3(\nu_o)/2 + \ln 2}{0.23 G - \ln 2} \right)^{1/2} \quad (27)$$

Thus, in addition to the increased small signal gain, the double-pass configuration yields a considerable increase in linewidth because of the increased saturation produced at the input (and output) end of the device.

3. Amplifier Design Procedure

In order to design a laser amplifier with the required performance characteristics, we require knowledge of the small signal gain coefficient α_o , the line center saturation intensity $I_s(\nu_o)$ and the linewidth $\Delta\nu$, as functions of pressure, current and tube diameter. By making use of these parameters in the analytical relationships derived in the previous section, we can calculate the minimum active device length required to achieve the overall design goals given earlier. This calculation can be repeated for a variety of experimental conditions, so that optimum conditions requiring the shortest amplifier length may be found. This approach will be followed in the full scale device characterization procedure given in Part F.

C. Test Bed Description

In designing a waveguide amplifier of 1 m nominal length, several problems are met. As a first consideration, it should be noted that ceramic sections with 1 to 2 mm drilled holes cannot be obtained in lengths greater than 5 to 6 in. Thus, in our device we have made use of a segmented design which incorporates seven separate ceramic (BeO) sections and connecting Kovar flanges. Each section is 5 in. long, with a 1.65 mm bore. The use of separate ceramic segments suggests a parallel connection of electrical power and gas flow, as represented schematically in Fig. 24 and shown in more detail in Fig. 25. The electrical connections are arranged so that all of the connecting flanges are grounded (for safety reasons) and the center electrodes serve as cathodes (to eliminate sputtering near the windows at each end). The 2 mm spacing between sections is large enough to allow adequate gas flow, but small enough to maintain a low theoretical value of optical loss (0.09%). Each segment is attached to a separate heat sink mount, which in turn is fastened to an I-beam support.

An important consideration in the amplifier construction is the mechanical alignment of the separate ceramic sections. Since the most relevant indication of alignment accuracy is given by the device transmission, it was felt that a continuous monitoring of transmission

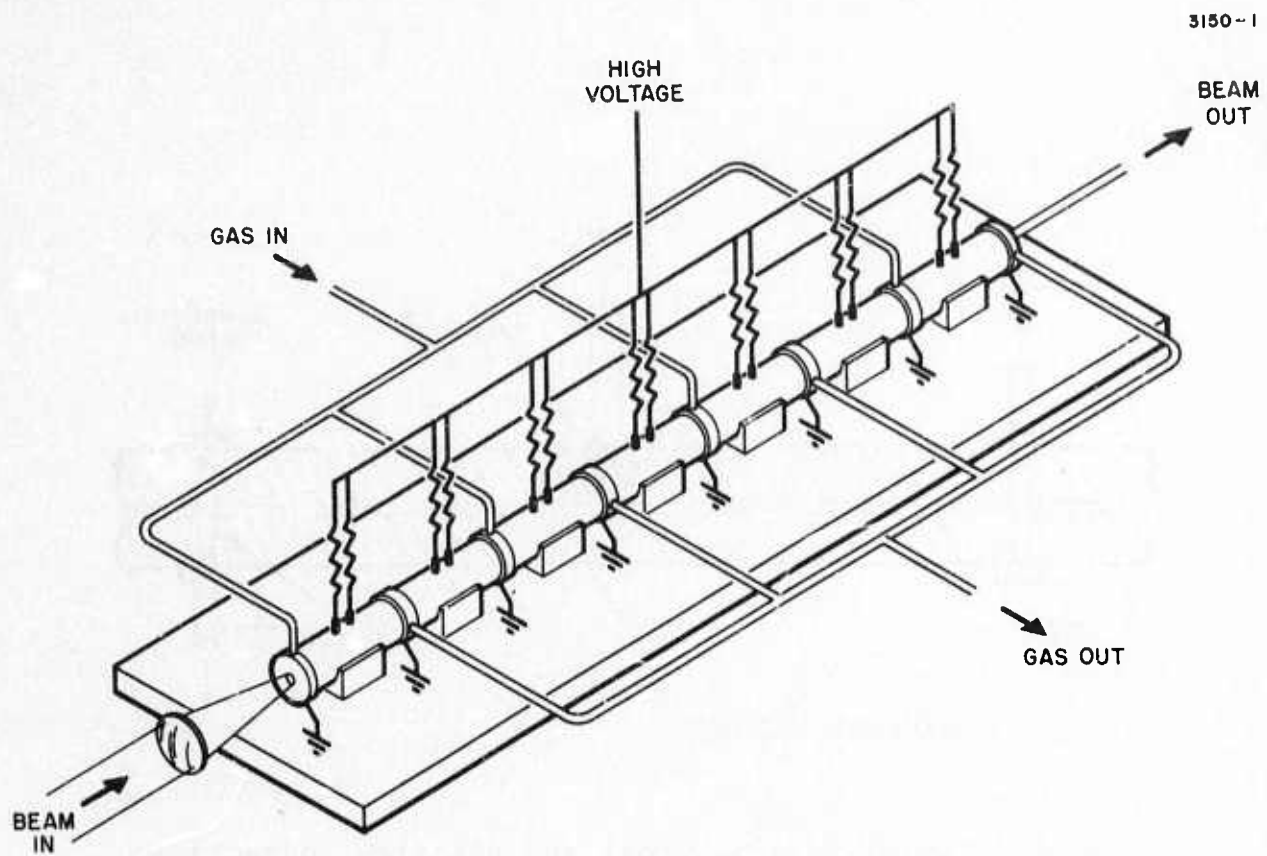


Fig. 24. Amplifier assembly.

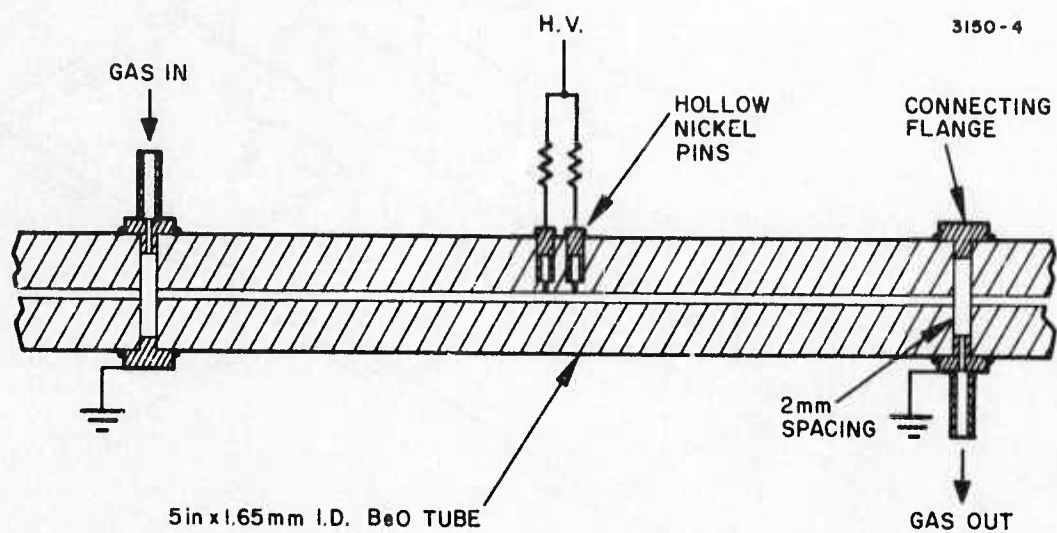


Fig. 25. Detail of electrical and gas flow connections.

during assembly was desirable. This was accomplished by first passing the beam from a 1-W CO_2 laser through a telescope adjusted to provide a spot size w at its focus which optimizes coupling into the EH_{11} waveguide mode. If a is the tube radius, then the required condition is $w = 0.6435 a$,⁵ corresponding to a coupling of 98%. When guiding losses and coupling losses at each joint are taken into account, we calculate a theoretical transmission for our device of 97%.

The alignment procedure of our device was initiated by clamping the first (input) ceramic section (and heat sink mount) to the I-beam, and aligning the monitor laser beam with the input aperture by optimizing transmitted power. As each ceramic section was added, its lateral position (at the connecting flanges) and angular alignment was adjusted to maximize the transmitted power at $10.6 \mu\text{m}$. As an auxiliary technique for optimizing positioning at the flanges, provision was also made for passing an unfocused 6328 \AA laser beam through the amplifier sections. With the room lights off, the scattered red light at each new joint was clearly visible, and reached a distinct minimum for optimum positioning. This visible laser technique was found to be the most useful for fine adjustment of positioning. After optimum positioning of the seven sections and fastening the heat sink mounts to the I-beam, we measured an overall $10.6 \mu\text{m}$ transmission of 92%, limited primarily by residual misalignment at the joints between sections. As the final step in the assembly the connecting (and end) flanges were epoxied to the ceramic; the Brewster window material was CdTe. A photograph of the completed device is shown in Fig. 26. When account is taken of spacing between sections and between cathodes, the total active device length is 77 cm (14 discharges \times 5.5 cm per discharge).

D. Gas Flow Considerations

As discussed earlier, the seven ceramic sections have parallel gas flow connections to minimize the pressure drop across the total device length. A schematic diagram of the gas flow system is given in Fig. 27. Helium, nitrogen and carbon dioxide in ultra-pure form

M10432

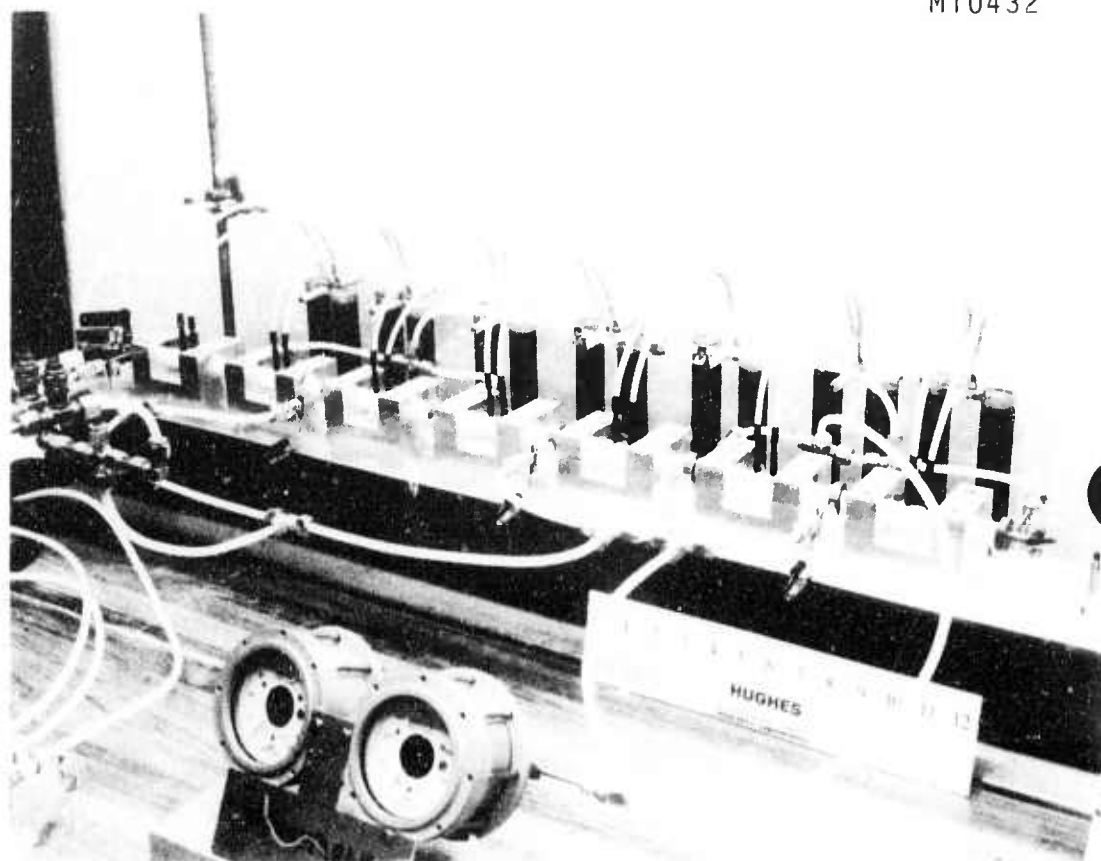


Fig. 26. Completed amplifier.

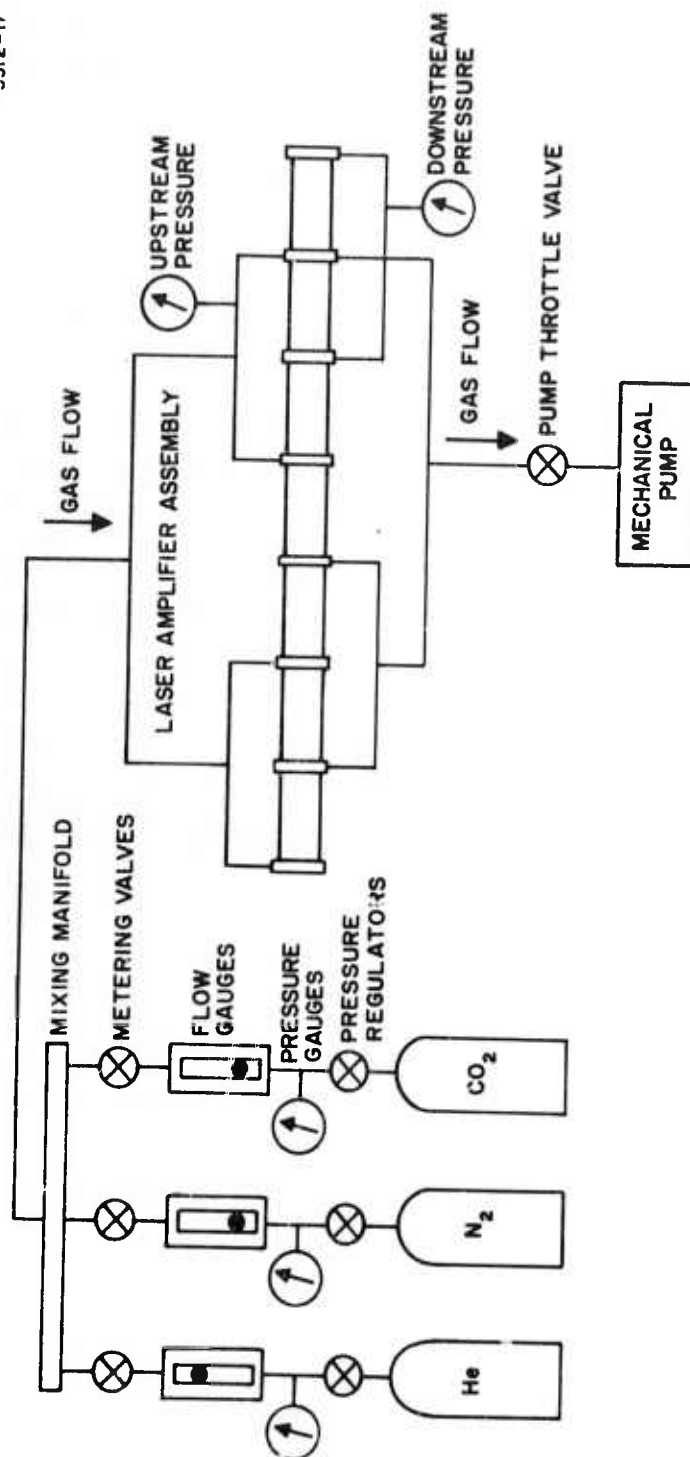


Fig. 27. Schematic diagram of gas flow system.

(99.999% purity) are fed from separate tanks through individual flowmeters and needle valves to a mixing manifold, and then into the discharge region. The flow then passes through a throttle valve (for control of the amplifier pressure) and is exhausted through a (Welch 1402) 5.6 cfm mechanical pump.

The gas flowmeters can be connected and calibrated to read mass flow (e.g., Torr-liters/s) or volumetric flow (e.g., liters/s). We feel that greater accuracy and ease in calibration is obtained by maintaining the flow tubes at constant pressure and regulating the flow with downstream needle valves (as shown in Fig. 27). In this mode of operation the flowmeter reading is proportional to mass flow. For the purpose of relating amplifier parameters to flow rates, the flow is best specified by the number of gas fill changes per second for each separate flow length. This quantity may then be compared directly to the rates of other relevant processes in the discharge. For the geometry of our flow system, we have

$$N = 5.33 \times 10^2 \frac{Q_T}{P_o} \text{ changes/s} , \quad (28)$$

where Q_T is the total mass flow in Torr-liters/s, and P_o is the average pressure in Torr.

E. Electrical Circuitry

As mentioned earlier, the separate ceramic sections each contain two centrally located hollow nickel cathodes. The Kovar connecting flanges serve as common anodes for adjacent discharges. The high voltage power supply (with positive ground) provides negative high voltage to the cathodes through separate $1 \text{ M}\Omega$ ballast resistors. The anodes are connected to ground through separate $1 \text{ k}\Omega$ resistors. The voltage drop across these resistors is a convenient measure of the discharge current.

Although the high voltage power supply has an option which provides rapid application of a preset voltage to the 14 amplifier discharges, simultaneous ignition of all discharges is very difficult to achieve except at low pressures, or in helium-rich mixtures. In order to avoid this problem, we have developed a unique starting system which provides reliable ignition of all discharges for the total range of typical pressures and mixtures. In our system (see Fig. 28) a high voltage pulse (60 kV) is series injected into the negative high voltage lead from the dc power supply when this supply is switched on. The triggering for the pulse generator is derived by sensing the voltage across several of the 1 K anode circuit resistors. These resistors are parallel connected, so that if any of the discharge circuits draws current (by discharge ignition), a trigger pulse is produced.

Either polarity of pulse voltage improves the starting performance of the discharges, with a positive polarity providing somewhat better reliability. In this case the rising portion of the high voltage pulse is assumed to extinguish any discharges which may have started prematurely, thus allowing the falling (increasingly negative) portion of the pulse to ignite all discharges simultaneously.

A schematic diagram of the starting circuit is given in Fig. 29. The negative pulse from the anode resistors is inverted by the input transformer T1 and is used to trigger the C6B SCR. The resulting pulse is amplified by the interstage transformer T2 and then is used to trigger the KN-4 cold cathode switch. The resulting discharge of the 10 μ F storage capacitor (charged to 720 V) through the primary of the transformer T3 produces a 60 kV, 10 μ s pulse at the secondary, which is injected into the cathode circuit of the amplifier discharges. The starter circuit also provides for manual initiation of the high voltage pulse, if automatic operation is not desired. This was used for starting of the tunable local oscillator, which has a similar electrode configuration.

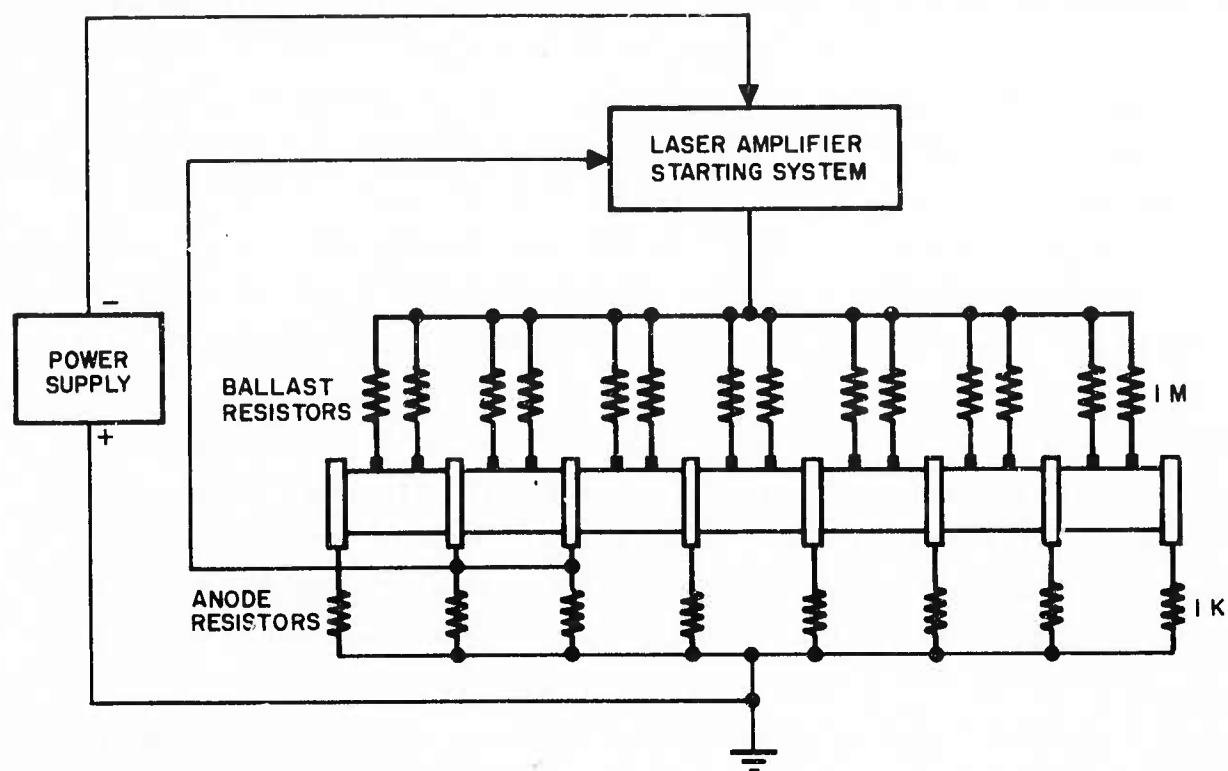


Fig. 28. Schematic diagram of electrical connections.

53

F. Experimental Results

In this section we report the results of measurements of small signal gain coefficient and saturation intensity for a variety of experimental conditions. The experimental arrangement for all optical experiments is identical. The source oscillator is a 1-W conventional bore CO₂ laser tuned to line center of the P(20) transition. The output from this laser is focused onto the entrance aperture of the first amplifier section by passing through a telescope adjusted for optimum coupling. A variable attenuator is also provided at the input to the amplifier. A power meter at the amplifier exit is used to measure transmitted power. In order to obtain the input power to the amplifier, the transmitted power through the passive amplifier (with 8% transmission loss) was multiplied by 1.08. The amplifier gain is then given by the ratio of the transmitted power through the active amplifier divided by input power as given above. In general, our gain measurements were performed using a constant input power of 100 mW in the expectation that saturation effects would be unimportant at this power level. Our subsequent measurements of saturation intensity (presented in a later section) indicate that this assumption is accurate at 150 Torr with small errors being introduced at lower pressures. However, even at 50 Torr, the discrepancy between the measured gain coefficient and the small signal gain coefficient using a 100 mW source is less than 10%.

During the course of our measurements, care was taken to ensure that spontaneous emission noise and absorption by the cold gas were negligible factors. We also examined the discharge voltage at various times for signs of high frequency oscillations and none were observed.

1. Small Signal Gain versus Flow Rate

Before proceeding with gain measurements as a function of pressure, it is important to know the effects of gas flow on the gain. We have measured gain versus gas flow (measured in changes/s) at three different pressures; the gas mixture at each pressure has been

adjusted for maximum gain. The results are shown in Fig. 30. The dashed line for each plot is an extension of the measured data to the sealed off measured values of Abrams and Bridges (Ref. 1). At each pressure the gain rises rapidly, and then approaches a constant value for flow rates greater than ~ 200 changes/s. All subsequent gain measurements have been performed at flow rates of this magnitude.

2. Small Signal Gain versus Pressure

In Fig. 31 we show values of gain measured as a function of pressure for gas mixtures optimized at 50, 100 and 150 Torr. The flow rate for all measurements was kept constant at 200 changes/s. For reference purposes the gain is given in %/cm, dB/m, and overall gain for the device under investigation. The displayed data was taken at 3 mA current. In general, the gain at 2 mA and 4 mA is slightly lower.

As expected, the gain for a given mixture decreases at pressures above optimum, and peaks at lower pressures (generally less than 50 Torr). The data of Fig. 28 does not extend below 50 Torr because we were not able to maintain the required flow rate in this range. However, measurements at approximately 120 changes/s yielded an overall gain of 17.5 at 38 Torr (in a 3:1:1 mixture), corresponding to gain coefficients of 3.7%/cm, or 16.1 dB/m.

3. Measurement of Saturation Intensity

Many techniques for measuring the saturation intensity (using both oscillator and amplifier configurations) are available, and we have chosen one which we feel is particularly suitable to our experimental conditions. We make use of the same laser source (tuned to line center) used in the gain measurements, and adjust the attenuator to provide a variable power input in the range 0.1 to 1.0 W. The relation describing the interaction of such a source in the amplifier is given by eq. (8), with $\delta = 0$.

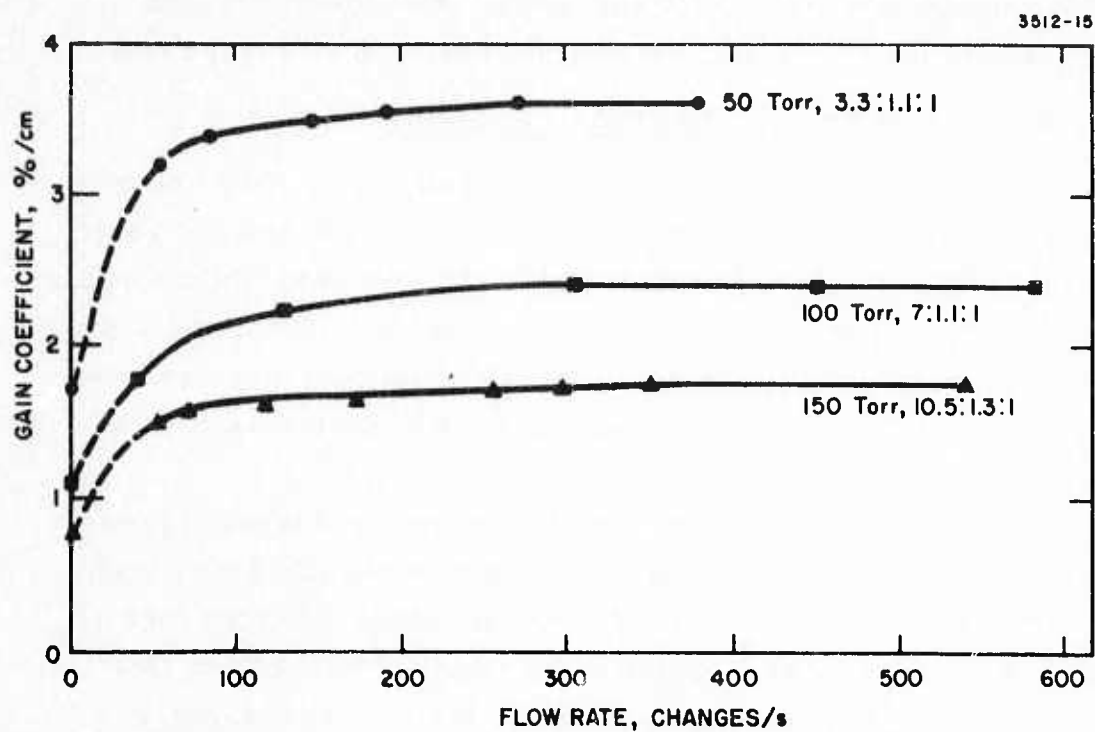


Fig. 30. Gain versus flow rate for 50, 100 and 150 Torr pressure. The gas mixtures are presented in the ratios He:Ne:CO₂. The discharge current was 3 mA.

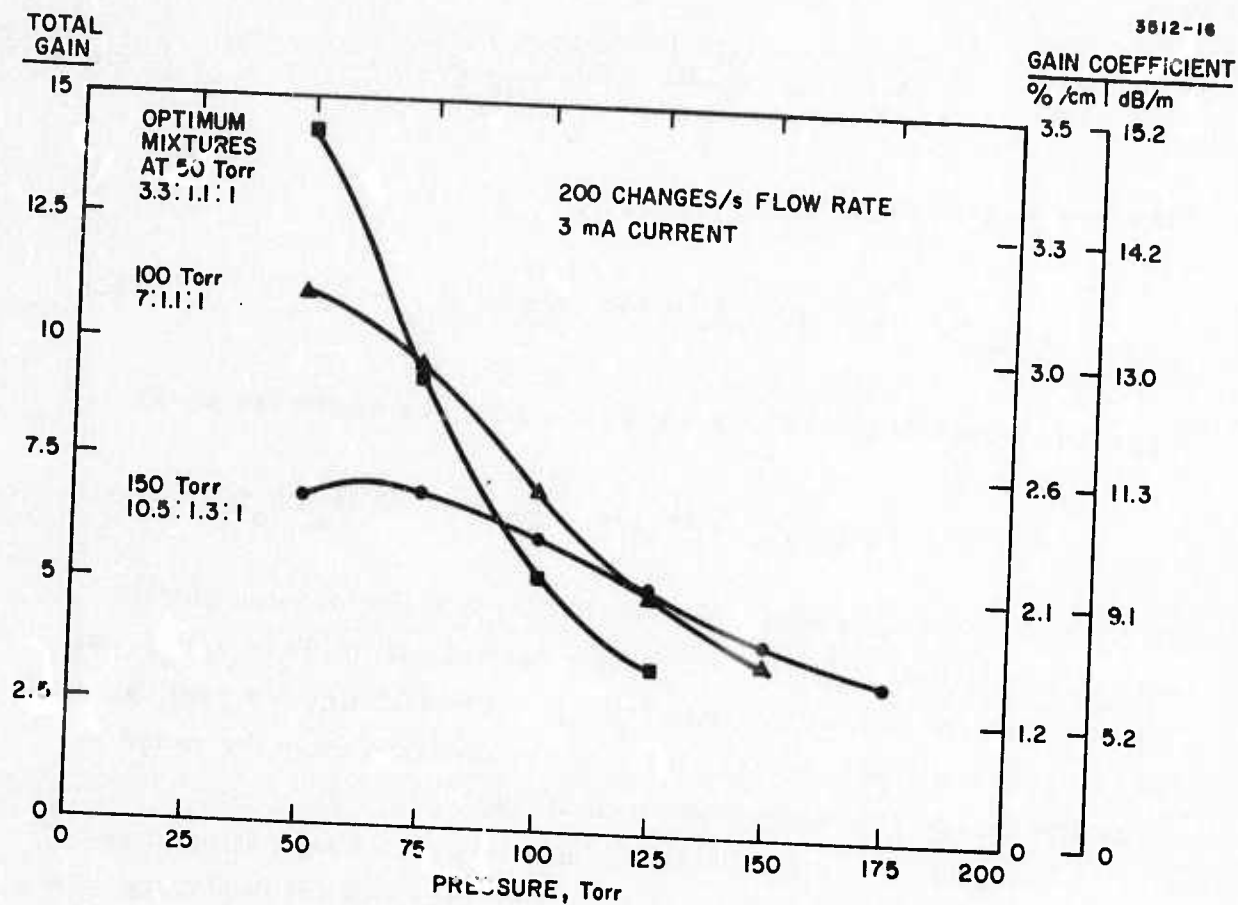


Fig. 31. Gain versus pressure at constant flow rate (200 changes/s) and current (3 mA).

$$\alpha_o L = \ln \frac{\gamma_2}{\gamma_1} + (\gamma_2 - \gamma_1) \quad (29)$$

or

$$\alpha_o L = \ln \frac{I_2(\nu_o)}{I_1} + \frac{I_2(\nu_o) - I_1(\nu_o)}{I_s(\nu_o)} \quad (30)$$

This may be rewritten as

$$I_2(\nu_o) - I_1(\nu_o) = -I_s(\nu_o) \ln \frac{I_2(\nu_o)}{I_1} + I_s(\nu_o) \alpha_o L \quad (31)$$

Written in terms of power instead of intensity, the above becomes

$$P_2(\nu_o) - P_1(\nu_o) = -P_s(\nu_o) \ln \frac{P_2(\nu_o)}{P_1} + P_s(\nu_o) \alpha_o L \quad (32)$$

Thus, by measuring output power $P_2(\nu_o)$ for a range of input powers $P_1(\nu_o)$ and plotting $P_2(\nu_o) - P_1(\nu_o)$ as a function of $\ln[P_2(\nu_o)/P_1]$, we obtain a straight line with slope $-P_s(\nu_o)$. This technique is applicable for any range of input powers, but is most accurate when the range is large and appreciable saturation is produced.

Using the above technique we have measured saturation power for five pressures in the range of 50 to 150 Torr and for discharge currents of 2, 3, and 4 mA. The gas mixture at each pressure is that which produces maximum gain. For each setting of pressure and current the data were plotted as described above. A straight line was then fitted (by the method of least squares) to each set of data points. An example of the plotted data (at 100 Torr) is given in Fig. 32. The saturation power was obtained from the slope of each curve, and is plotted as a function of pressure (for each current) in Fig. 33. The saturation intensity may be obtained by dividing the power by πw^2 , where w is the e^{-1} intensity radius of the Gaussian beam which best matches⁵ the EH_{11} waveguide mode ($w/a = 0.455$).

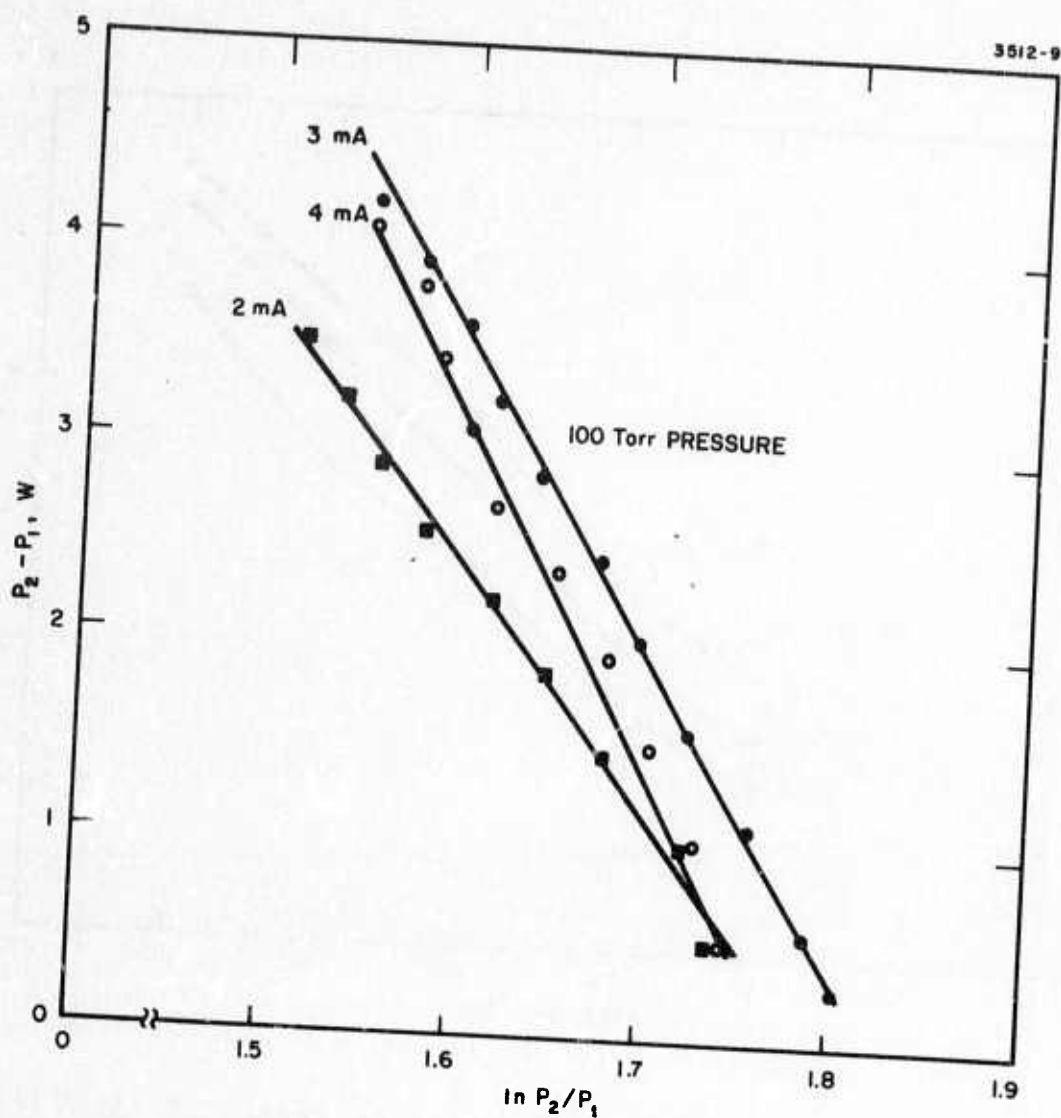


Fig. 32. Graphical technique for measuring saturation power. The gas mixture is set for maximum gain.

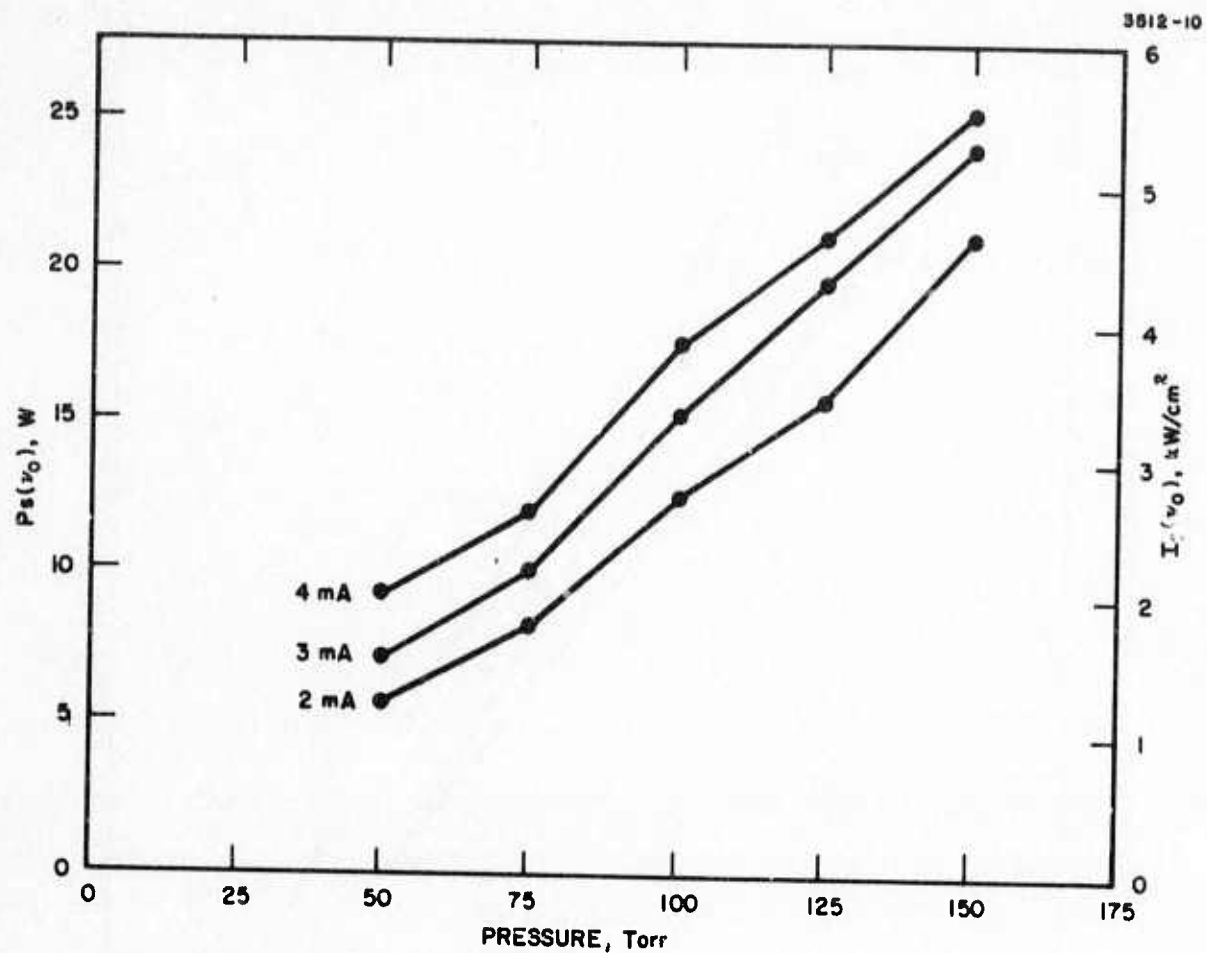


Fig. 33. Saturation power and intensity versus pressure (flow rate = 500 changes/s).

As expected, the saturation intensity increases with pressure (due to molecule-molecule collisions) and with current (due to electron molecule collisions). The values of this parameter are approximately a factor of two lower than the measured values of Abrams and Bridges¹ for a sealed off oscillator using He-CO₂ mixtures. The reasons for this discrepancy are not well understood, although it is felt that the gas mixtures which produce optimum gain may not produce the largest value of saturation intensity.

In a highly saturated amplifier, one relevant measure of device performance is the power extraction capability (in W/m), given by the product of small signal gain coefficient and the saturation power. In Fig. 34, we plot values of $\alpha_o P_s(\nu_o)$ as a function of pressure (at 3 mA current) using previously plotted values of gain and saturation power. We have also plotted measured values of electrical input power per unit length for the same conditions.

The values of available power per unit length given in Fig. 34 are approximately a factor of two lower than those calculated by Abrams and Bridges (Ref. 2) from gain and saturation measurements in a sealed off 1.5 mm tube, but are about twice the value they obtained from laser output power measurements. It is clearly desirable to find a means for increasing the available output power (and input electrical power) in our device. The most direct technique for doing this would be to operate the amplifier discharge as an oscillator, and adjust mixtures, pressure and current for maximum power output. As mentioned earlier, it is likely that the particular mixtures which optimize output power will not be the same as those which optimize gain alone.

G. Characterization of Full Scale Device

On the basis of the measurements described in the preceding sections, we are in a position to determine the amplifier length required to meet the program goals discussed earlier. The length is related to other amplifier parameters by

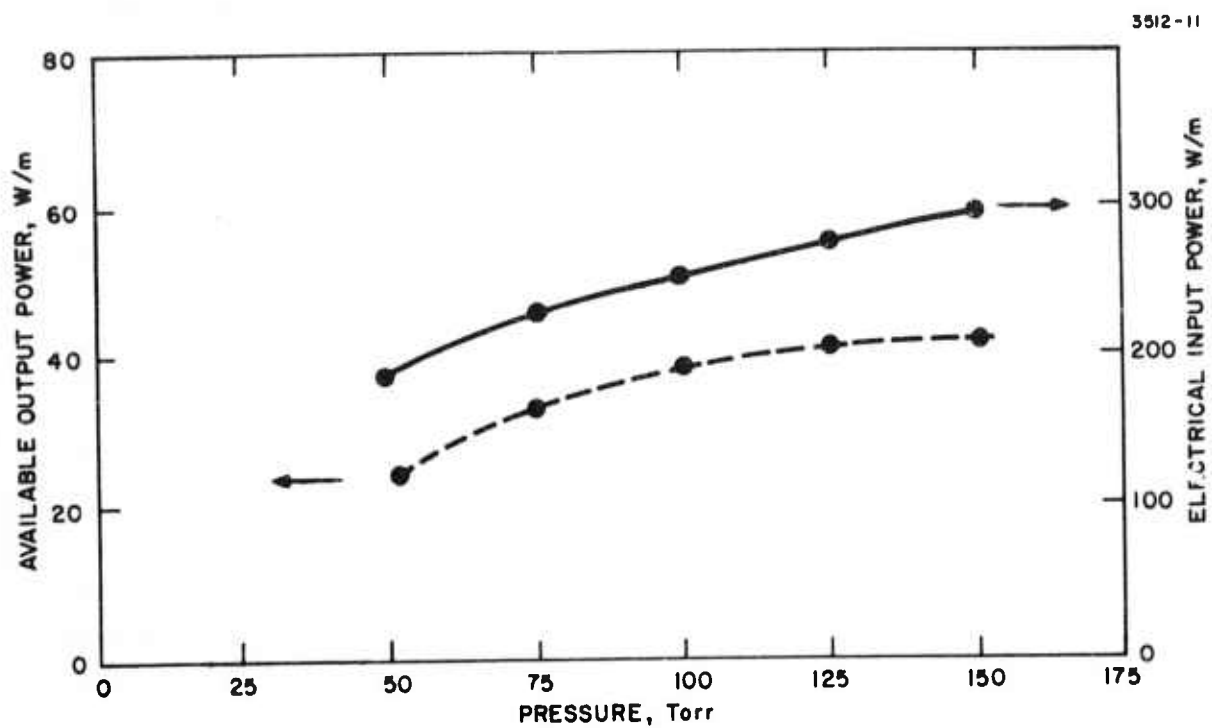


Fig. 34. Available output power and input electrical power versus pressure. Discharge current = 3 mA.

$$a_o L = \gamma_2(\nu_o) + \ln \frac{\gamma_2(\nu_o)}{\gamma_1} \quad (33)$$

Solving for L and writing in terms of power instead of intensity we obtain

$$L = \frac{1}{a_o} \left[\frac{P_2(\nu_o)}{P_s(\nu_o)} + \ln \frac{P_2(\nu_o)}{P_1} \right] \quad (34)$$

In Fig. 35 we have made use of the above expression to plot the required length L as a function of line center output power $P_2(\nu_o)$ for three different pressures, using the gain and saturation power data of previous sections. We have assumed a constant 1 W input and a discharge current of 3 mA. The curves for 2 and 4 mA are very close to those plotted in Fig. 35. It should also be noted that the straight line nature of the plots in Fig. 35 follows directly from differentiation of eq. (34), in the limit $P_2(\nu_o) \gg P_s(\nu_o)$. The slope of each plot is just $[a_o P_s(\nu_o)]^{-1}$, or the inverse of the extractable power per unit length.

Using eq. (13) we have also calculated the 3 dB amplifier line-width for the range of parameters plotted in Fig. 35. We find that at 150 Torr, $\Delta\nu_{3 \text{ dB}} > 500 \text{ MHz}$ for the entire plotted range of output powers. At 100 Torr pressure, $\Delta\nu_{3 \text{ dB}} > 500 \text{ MHz}$ for output powers greater than 80 W. Finally, at 50 Torr we find $300 < \Delta\nu_{3 \text{ dB}} < 500 \text{ MHz}$ over the entire plotted range of output powers. In each of these cases, the amplifier is strongly saturated at the output, resulting in significant power broadening of the amplifier bandwidth.

We see from Fig. 35 that the optimum amplifier pressure over the plotted range of output powers is near 100 Torr. However, even at the optimum pressure, the required lengths range from 3 m (for 17 dB overall gain) to 7 m (for 23 dB overall gain). Thus, the required amplifier length depends critically on the final design value of the required system gain. If this parameter can be relaxed somewhat from a value of 20 dB, or if a higher power local oscillator is available, the requirements on amplifier length are reduced considerably.

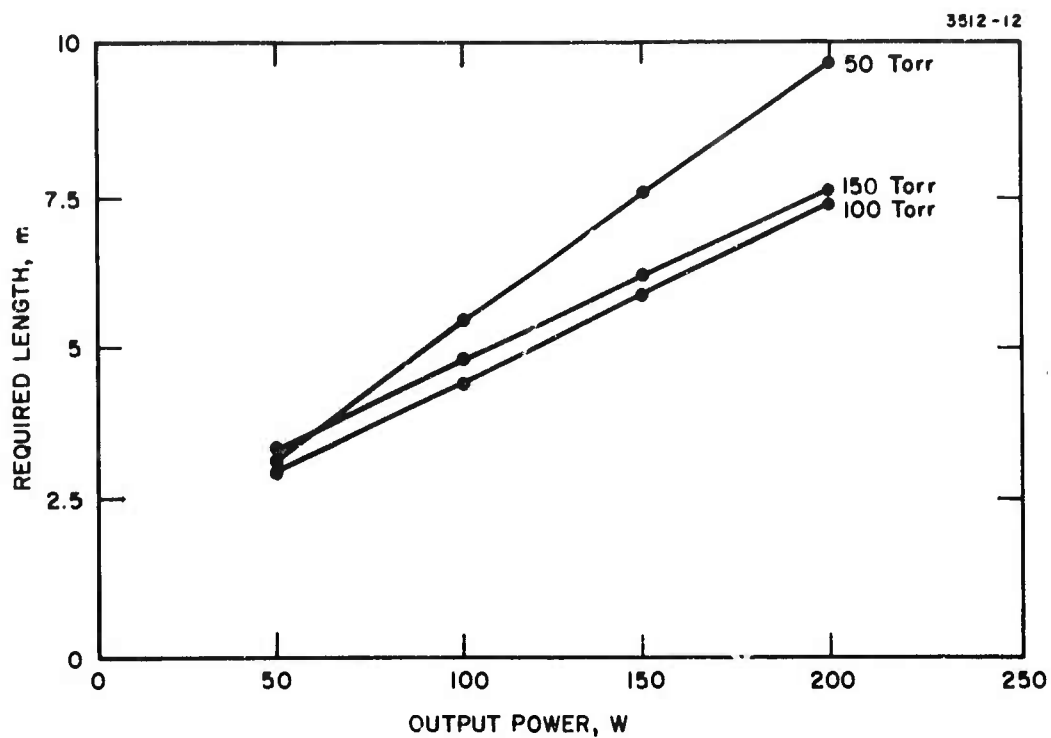


Fig. 35. Required length as a function of output power for a 1 W input.

There are several further refinements which can be made to further improve the amplifier performance. Most importantly, cooling of the amplifier is known to produce a significant improvement in small signal gain coefficient, with a 50% increase at -60°C being typical (Ref. 3). Secondly, as discussed earlier, it is possible that different gas mixtures exist at each pressure which produces higher values of saturation intensity and extractable power. Finally, a double-pass configuration may be used to provide length reductions approaching a factor of two.

REFERENCES

1. R.L. Abrams and W.B. Bridges, IEEE J. Quantum Electron. QE-9, 940 (September 1973).
2. E.A.J. Marcatili and R.A. Schmelzter, Bell Syst. Tech. J. 43, 1783 (July 1964).
3. T.J. Bridges, E.G. Burkhardt, and P.W. Smith, Optics Communications 6, 193 (1972), and Appl. Phys. Lett. 20, 403 (1972).
4. J.J. Degnan, J. Appl. Phys. 45, 257 (1974).
5. R.L. Abrams, IEEE J. Quantum Electron. QE-8, 838 (November 1973).

APPENDIX A

WAVEGUIDE LOSSES

In order to insure efficient operation of a waveguide gas laser, it is essential to keep guiding losses as small as possible. For a waveguide bore with a smooth, straight interior surface, the losses are due only to leakage into the guiding medium from the bore. For the lowest order EH_{11} mode the loss coefficient may be written as^{A-1}

$$\alpha_{11} = \left(\frac{2.405}{2\pi} \right)^2 \frac{8\lambda^3}{D^3} \operatorname{Re}(\nu_n),$$

where D is the bore diameter and ν_n is an expression involving the complex index of refraction of the wall material $\nu = n - ik$,

$$\nu_n = \frac{1/2(\nu^2 + 1)}{(\nu^2 - 1)^{1/2}}$$

Thus, for a given bore radius and wavelength, the best bore material is one whose optical constants yield the smallest value^{A-2} of $\operatorname{Re}(\nu_n)$. Of all the potential bore materials, the one with the smallest value of $\operatorname{Re}(\nu_n)$ at 10.6μ is BeO. For this material we find $\alpha_{11} = 4.3 \times 10^{-5} \text{ cm}^{-1}$ for a 1-mm diameter waveguide at 10.6μ ; other potential bore materials such as alumina, quartz or pyrex all yield loss coefficients on the order of $2 \times 10^{-3} \text{ cm}^{-1}$.

As mentioned earlier, there are two effects which can produce an increase in waveguide loss over the ideal case as given in eq. (1). The first is a lack of straightness of the waveguide bore. Marcatili and Schmeltzer^{A-1} have shown that for a waveguide with uniform bend radius R , the loss coefficient for the EH_{11} mode is given by

Preceding page blank

$$\alpha(R) = \alpha(\infty) \left\{ 1 + 4/3 \left(\frac{2\pi a}{2.405 \lambda} \right)^4 \cdot \left(\frac{a}{R} \right)^2 \left[1 + \frac{1}{(2.405)^2} + \frac{3}{4} \frac{\operatorname{Re}(\sqrt{v^2 - 1})}{\operatorname{Re}(\frac{v^2 + 1}{\sqrt{v^2 - 1}})} \cos 2\theta_0 \right] \right\}$$

Here $\alpha_{11}(\infty)$ is the loss coefficient for a straight guide, a is the bore radius, and θ_0 is the angle between the mode polarization and the plane of bending. For example, a 60 m radius bend in a 1.5 mm BeO waveguide increases the straight guide loss by 17 to 41%, depending on the polarization orientation.

A second potential contribution to the waveguide loss arises from the departure from ideal smoothness of the interior bore surface. It is expected that a rough surface will scatter more light out of the specular direction than a smooth surface, thereby lowering the waveguide transmission. The strength and functional dependence of this effect are considered in detail in subsequent sections.

1. Effects of Surface Roughness on Specular Reflectivity

The propagation of a guided mode through a waveguide laser bore may be considered to proceed via a series of grazing incidence specular reflections from the interior wall surface. If one can predict the intensity loss for each wall reflection, then the loss of each mode can be obtained from the angle of incidence and number of reflections. A convenient expression for specular reflectivity as a function of roughness and angle also permits a convenient optical measurement of the surface roughness of flat samples.

The most comprehensive theory relating reflectivity to surface roughness is given by Beckmann.^{A-3} In this treatment the surface is considered to possess a statistical distribution of surface heights $w(z)$, where $w(z)$ is the probability of measuring a height z above the plane $z = 0$, and is characterized by a correlation distance T , which is a measure of the roughness density on a horizontal scale.

By applying diffraction theory in the Kirchhoff approximation, Beckmann obtains an expression for the amplitude reflectivity ρ of a rough surface in the specular direction:

$$\rho = \int_{-\infty}^{\infty} w(z) e^{ik_z z} dz. \quad (A-1)$$

In this expression we have

$$k_z = \frac{4\pi}{\lambda} \cos \theta, \quad (A-2)$$

where θ is the angle of incidence. It may be seen from eq. (A-1) that the amplitude reflectivity is just the Fourier transform of the surface height distribution function.

The intensity reflectivity is related to the amplitude reflectivity by

$$R = \langle \rho \rho^* \rangle. \quad (A-3)$$

The reflectivity as given here is applicable to rough metal surfaces, where the reflectivity in the absence of roughness is unity. In the case of a rough dielectric surface, the above expression is modified in a straightforward way to yield

$$\frac{R}{R_o} = \langle \rho \rho^* \rangle \quad (A-4)$$

where R_o is the reflectivity of a smooth surface of the same material. In cases where the optical constants of the bulk material are known, R_o may be calculated directly from the Fresnel equations.

For a given surface height distribution $w(z)$, the above relations may be used to derive an expression for the reflectivity ratio R/R_o as a function of θ , λ and σ . One commonly encountered distribution is the so-called normal (gaussian) distribution given by

$$w(z) = \frac{1}{\sigma \sqrt{2\pi}} e^{-z^2/2\sigma^2} \quad (\text{A-5})$$

By substitution into eqs. (A-1) and (A-4), we obtain

$$\frac{R}{R_o} = e^{-\left(\frac{4\pi\sigma\cos\theta}{\lambda}\right)^2} \quad (\text{A-6})$$

We may also consider a Lorentzian distribution for $w(z)$, given by

$$w(z) = \frac{\sigma}{\pi} \frac{1}{\sigma^2 + z^2} \quad (\text{A-7})$$

In this case we find

$$\frac{R}{R_o} = e^{-\frac{8\pi\sigma}{\lambda} \cos\theta} \quad (\text{A-8})$$

It may be seen from eqs. (A-6) and (A-8) that for $\sigma\cos\theta \rightarrow 0$, we obtain $\langle \rho \rho^* \rangle \rightarrow 1$. This result is, in fact, valid for any (normalized distribution $w(z)$ as seen from eq. (A-1) with $k_z = 0$, and may be derived independently of any restrictions on σ or T . This is a very powerful result since even for rough surfaces ($\sigma \approx \lambda$), the specular reflectivity still approaches unity at grazing incidence. Experimental results to be described later support this conclusion.

2. Effects of Surface Roughness on Waveguide Loss

In this section we derive expressions which will be used to discuss the effect of wall roughness on losses in one-dimensional waveguides, in line with Beckman's theory^{A-3} of the modification of the the path shown in Fig. A-1, the intensity in the guide is diminished by formulae for the TM and TE reflectivities r_{TM}^o and r_{TE}^o of a smooth surface at glancing incidence. The rough surface reflectivities for TM and TE polarizations are obtained by multiplication of the Beckmann factor, so that

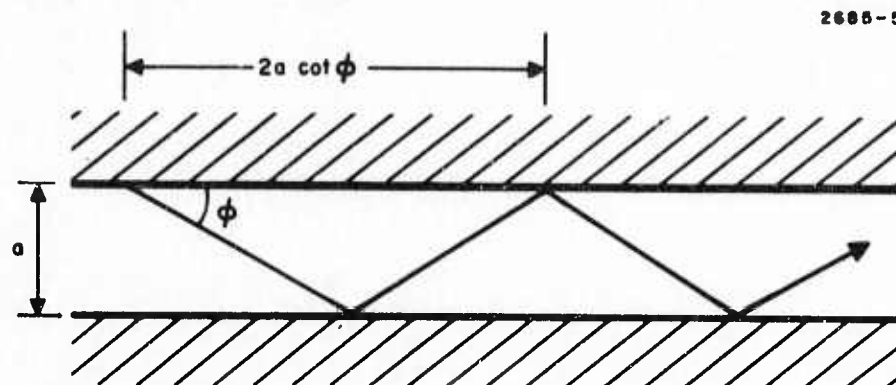


Fig. A-1. Ray optics view of planar waveguide mode.

$$r_{TE, TM} = r_{TE, TM}^0 e^{-\left(\frac{4\pi\sigma \sin \phi}{\lambda}\right)^2}$$

where ϕ is the glancing angle, and we have assumed a gaussian surface height distribution.

Fresnel's equation for a medium of indices (n_1, k_1) give for the reflectivities r_{TM}^0 and r_{TE}^0 :

$$r_{TM}^0 = \frac{(n_1 \sin \phi - 1)^2 + k_1^2 \sin^2 \phi}{(n_1 \sin \phi + 1)^2 + k_1^2 \sin^2 \phi}$$

$$r_{TE}^0 = \frac{(n_1 \sin \phi - 1)^2 + k_1^2 \sin^2 \phi}{(n_1 + \sin \phi)^2 + k_1^2}$$

For small ϕ , and using the condition $n_1 \gg k_1$, we derive approximations for r_{TM}^0 and r_{TE}^0 :

$$r_{TM}^0 \doteq 1 - 4n_1 \phi$$

$$r_{TE}^0 \doteq 1 - \frac{4n_1 \phi}{n_1^2 + k_1^2}$$

The Beckmann modification of r_{TM}^0 and r_{TE}^0 for a normally distributed rough surface is thus

$$r_{TM} = (1 - 4n_1 \phi) e^{-\left(\frac{4\pi\sigma \phi}{\lambda}\right)^2}$$

$$r_{TE} = \left(1 - \frac{4n_1 \phi}{n_1^2 + k_1^2}\right) e^{-\left(\frac{4\pi\sigma \phi}{\lambda}\right)^2}$$

We now derive an expression for the waveguide losses in terms of wall reflectivity, waveguide thickness, and grazing angle ϕ . For the path shown in Fig. A-1, the intensity in the guide is diminished by $1 - r^2$ over the path length $2a \cot \phi$, so for the low loss TE and TM modes,

$$\alpha_{\text{TE, TM}} = (1 - r_{\text{TE, TM}}^2) / 2a \cot \phi .$$

The angle ϕ is determined from the phase condition

$$\left[\frac{2\pi}{\lambda} \sin \phi \right] a = 2\pi(\nu+1)$$

where ν is the mode index. Therefore, for small ϕ

$$\cot \phi = \frac{a}{\lambda(\nu+1)} .$$

For the case of small σ , simplifications in the expressions for absorption may be made with the result

$$\alpha_{\text{TM}} = \frac{(\nu+1)^2 \lambda^2 n_1}{a^3} \exp \left[2(4\pi\sigma\phi/\lambda)^2 \right] = \alpha_{\text{TM}}^0 \exp \left[2(4\pi\sigma\phi/\lambda)^2 \right]$$

$$\alpha_{\text{TE}} = \frac{(\nu+1)^2 \lambda^2 n_1}{a^3 (n_1^2 + k_1^2)} \exp \left[2(4\pi\sigma\phi/\lambda)^2 \right] = \alpha_{\text{TE}}^0 \exp \left[2(4\pi\sigma\phi/\lambda)^2 \right],$$

As a check with the more conventional derivation of Marcuse^{A-4} we present Marcuse's approximation for α_{TE}^0 of a smooth planar guide:

$$\alpha_{\text{TE}}^0 = \frac{(\nu+1)^2 \lambda^2}{a^3 \sqrt{n^2 - 1}}$$

Both approaches yield quite similar results when we put $\sigma = 0$ (smooth guides), but our results are directly applicable to discussions of the effects of wall roughness on laser performance, when viewed according to Beckmann's theory.

3. Experimental Results for Waveguide Loss

In this section we will describe several experiments intended to determine the influence of interior wall surface quality on the transmission of typical laser bores. Included in these experiments are studies of flat ceramic surfaces, loss measurements in one dimensional glass waveguide structures of known surface quality, and loss measurements in circular pyrex, quartz, and BeO laser waveguides. Besides providing useful information on the importance of wall scattering, the results of this section also help to identify other types of imperfections leading to increased guiding losses.

a. Studies of Flat Ceramic Surfaces - In order to characterize and specify the quality of the interior walls of waveguide laser structures, we have performed extensive studies of polished and unpolished flat ceramic surfaces of alumina and beryllium oxide. We have made use of three techniques for studying these surfaces: scanning electron microscope (SEM) photographs, mechanical surface profile measurements, and optical reflectivity measurements.

The ceramics used in laser structures are manufactured by mixing fine particles of the material with a binder and then compressing and/or firing the sample to remove the binder. This process also fuses the material and promotes grain growth; typical grain sizes are in the range of 1 to 5 μ . The uniformity and quality of the ceramic are determined largely by the compression and firing. If those processes are not accomplished satisfactorily, the material will contain pores which will limit the quality of a polished surface. Furthermore, the average grain size of the material is a significant parameter, since it determines the lateral roughness scale of the ceramic surface.

Figure A-2 is an SEM photograph of a flat BeO surface comparable in quality to that encountered on the interior of our laser structures. Our laser bores are produced by a grinding operation using a thin drill; the sample surface shown here has been machined flat from the same material. The surface structure here is quite chaotic, with a scale of variation comparable to the expected grain size. In order to

2685-12

5 μ m

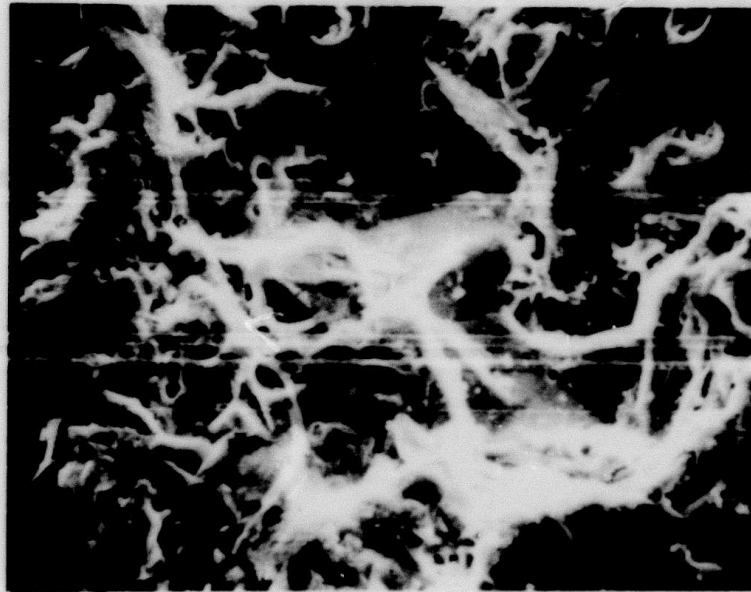


Fig. A-2. SEM photograph of machined beryllia surface.

determine the vertical roughness a scale of this same sample, we have mechanically examined its surface using a Dektak surface profile machine with a 30- μ diameter stylus; a typical scan is shown in Fig. A-3. We see here that the surface possesses peak-to-peak excursions of approximately 5 μ , with an rms value of approximately 1 μ .

By comparison with the previously measured sample, we show in Fig. A-4 an SEM photograph (at the same magnification as Fig. A-1) of an alumina surface which has been polished in our optical shop; a corresponding Dektak scan is shown in Fig. A-5. This surface is nearly free of pores and has been polished to an rms flatness of approximately 30 Å. We have found that the BeO samples studied tend to be relatively porous, thus limiting the finish of a polished surface to approximately 200 Å.

Another important technique for examining rough surfaces is the study of optical specular reflectivity. Previously, expressions were obtained for the reflectivity ratio R/R_0 as functions of σ , λ and θ for two common surface height distributions. Other distributions yield different functional dependences but they all yield unity reflectivity as $\sigma \cos \theta / \lambda$ approaches 0. The most convenient way to verify this dependence is to measure the specular reflectivity R as a function of angle, and plot the logarithm of the reflectivity ratio R/R_0 versus $\cos^2 \theta$ (assuming a gaussian distribution) or $\cos \theta$ (assuming a Lorentzian distribution). If a straight line is obtained in either case, then the slope may be related directly to the roughness σ . Even if some other distribution is applicable, a plot of reflectivity versus $\cos \theta$ (or $\cos^2 \theta$) should extrapolate to 1 for $\cos \theta = 0$.

Typical results for two samples are shown in Fig. A-6. Sample A is the same BeO surface studied earlier (see Figs. A-2 and A-3), and sample B is a second BeO surface with a crude polish. The results are plotted versus $\cos \theta$, since sample B fits a straight line very well in this case. If we assume sample B to be characterized by a Lorentzian distribution of surface heights, we obtain (from the slope) the value of σ shown. In the case of sample A, the indicated value of σ was obtained from the average slope and is in good agreement with this

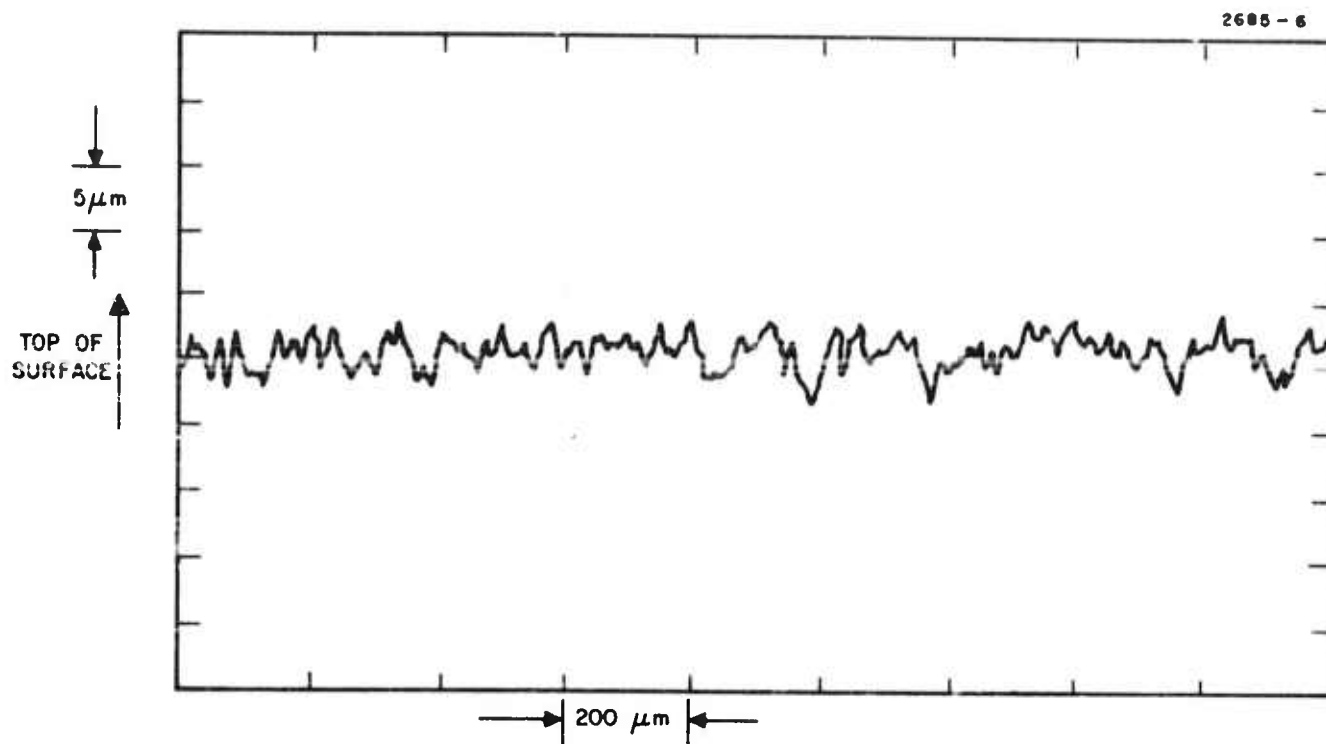


Fig. A-3. Surface profile scan of machined beryllia surface.

2685-11

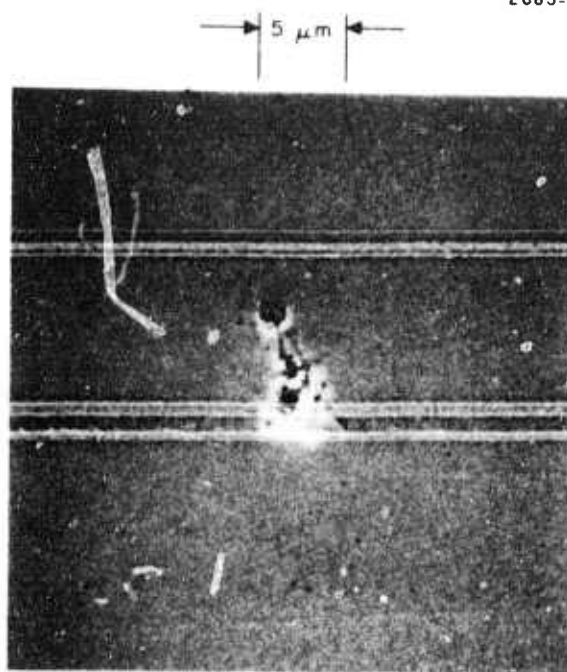


Fig. A-4. SEM photograph of polished alumina surface.

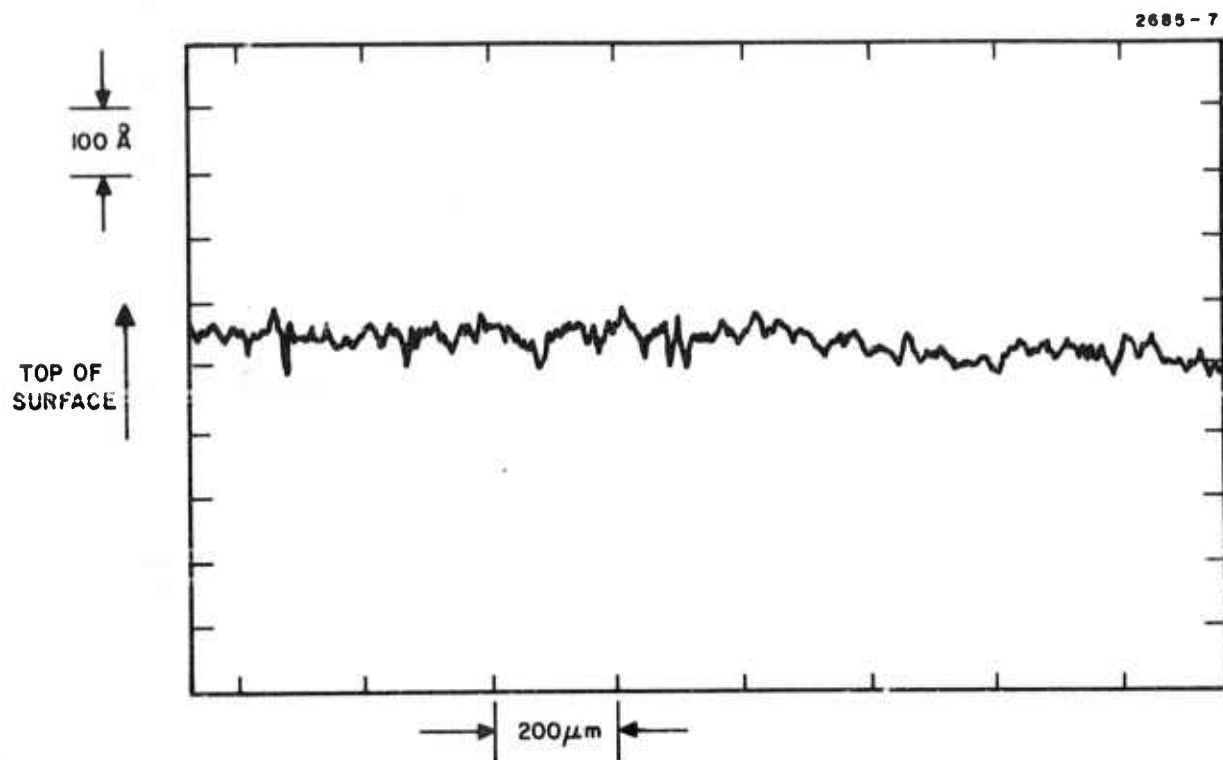


Fig. A-5. Surface profile scan of polished alumina sample.

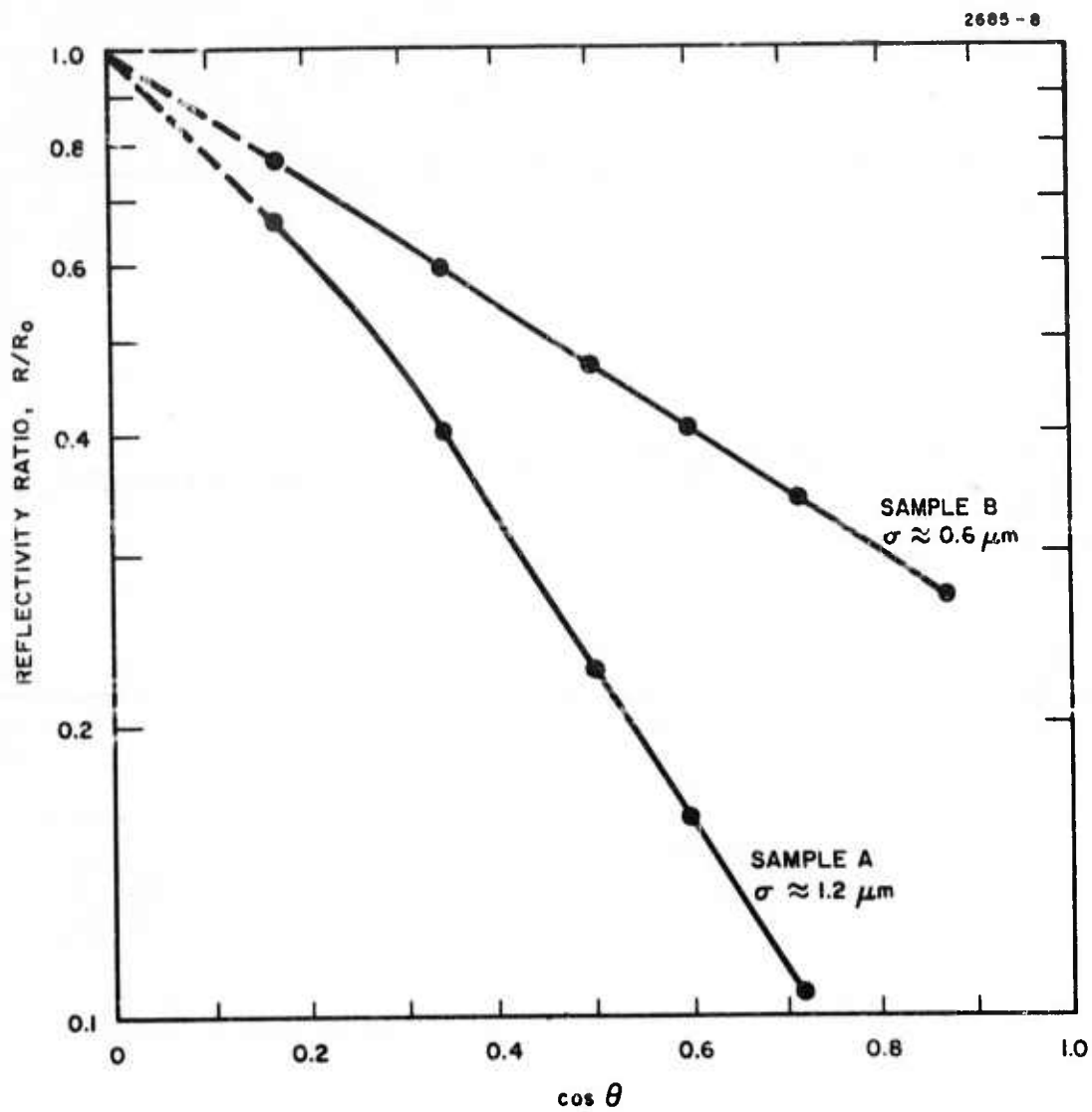


Fig. A-6. Reflectivity ratio R/R_0 versus $\cos \theta$.

Dektak value. In both cases the curves extrapolate very close to unity at $\cos \theta = 0$ (grazing incidents), in spite of the minimal polish which the surfaces possess.

It is important to note that the smooth surface reflectivity $R_o = R_o(\theta)$ used in the above analysis has been obtained by substitution of measured optical constants⁵ of single crystal BeO (at 10.6μ) into the Fresnel equations. We had hoped to perform an independent measurement of those constants for our ceramic samples by measuring $R(\theta)$ on highly polished surfaces, for which $R \approx R_o$; in this case the optical constants n and k could be determined (using the Fresnel equations) from reflectivity measurements at two different angles. Unfortunately, we were unable to obtain surfaces of sufficient smoothness to make meaningful measurement. However, our best surfaces provide apparent optical constants in close enough agreement with single crystal values to justify using the latter; this practice is also common in previous literature.^{A-6}

b. Circular Waveguide Loss Measurements -

Waveguide transmission measurements were made of actual waveguide laser structures of BeO and of quartz and pyrex waveguides of various diameters (1 mm, 0.8 mm, and 0.5 mm). We will first describe the experimental procedures employed and then summarize our results.

While the actual transmission measurements are straightforward, special care was given to the aligning of the samples with respect to the input beam and the matching of the CO_2 laser beam waist to the sample diameter to afford optimum coupling to the lowest order EH_{11} mode. A Lansing mirror mount was adapted to accommodate the laser tubes. This apparatus, when placed on a vertical-horizontal translator, served well to position and align the samples with respect to the laser input beam. As evidence of the necessity to position and align the tubes carefully, Fig. A-7 shows two photographs of the far-field pattern as observed on thermographic paper when only slight misalignment occurs. The far-field pattern for a well aligned sample is shown for the sake of comparison. In all the experimental results

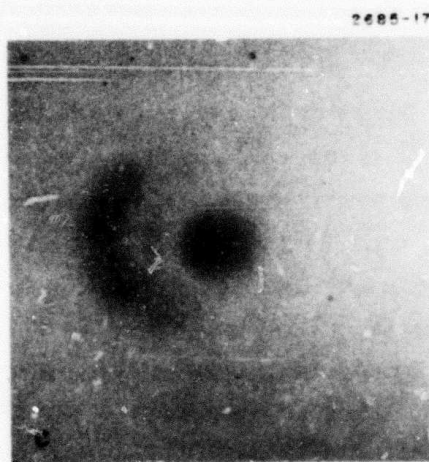
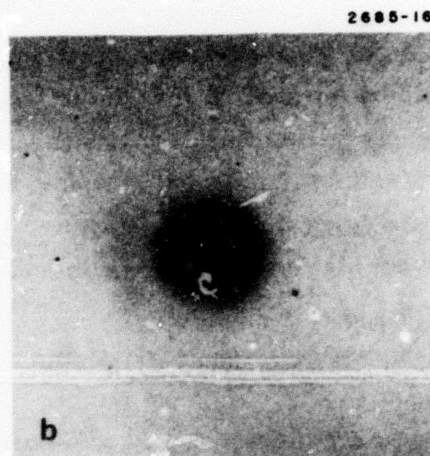
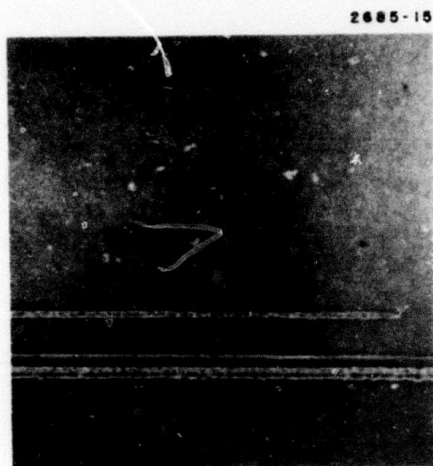


Fig. A-7. Far field radiation patterns for (a) null aligned, (b) slightly misaligned, and (c) misaligned waveguide.

we report, the input beam radius at its waist was adjusted to $0.6435 a$, where a is the tube radius. This optimum matching condition was previously derived by Abrams.^{A-7} For such a beam, 98% of the input beam is coupled to the EH_{11} mode and 99.3% of the total power is coupled into the waveguide. Throughout our experiments a 2 W single mode CO_2 laser which had been stabilized to within 1% variation was used.

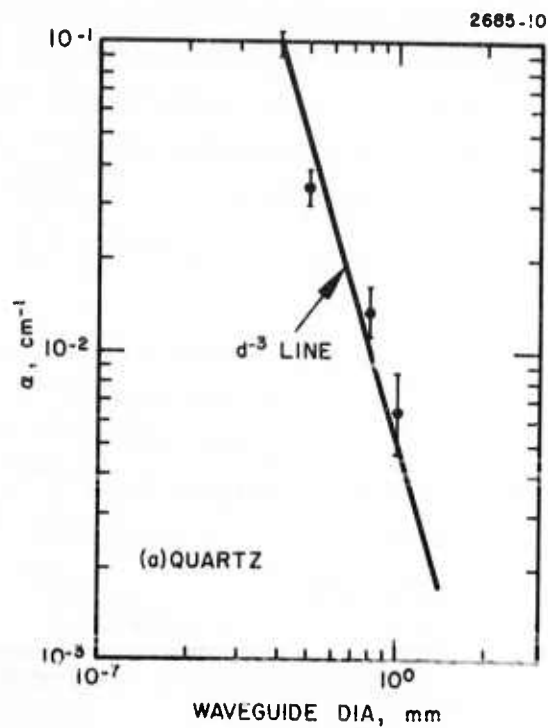
Waveguide transmission measurements were performed on quartz and pyrex precision bore tubing obtained from Wilmad Glass Company. The tubes for which measurements were made were of 0.4, 0.5, 0.8, 1.0 mm in diameter and 15.5 cm in length. The bore tolerances quoted by the manufacturer are ± 0.005 mm. No special effort was made to assure extremely straight tubes.

The transmission was measured first for the original length and later for smaller lengths obtained by carefully breaking the tubes. From the plots of transmission versus length and using the known coupling factor to the EH_{11} mode, the waveguide losses for this mode are calculated. These measurements are summarized for waveguides of quartz and pyrex of various diameters in Fig. A-8.

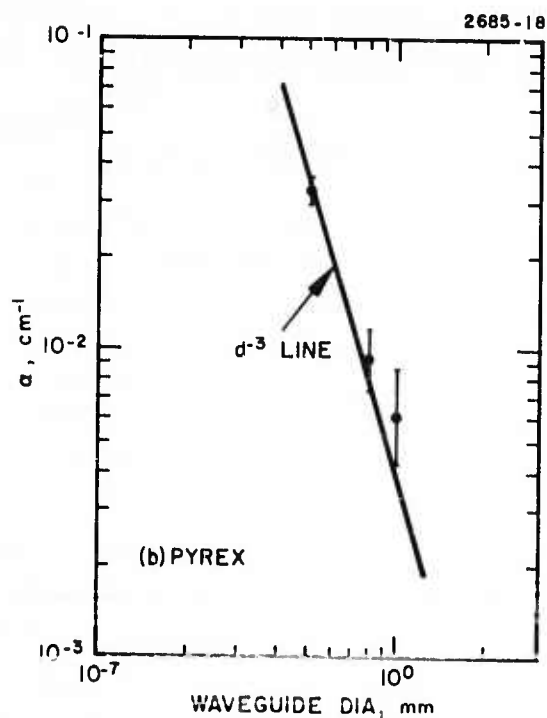
Two conclusions can be made based on these results:

1. The theoretically predicted d^{-3} behavior of the waveguide losses is directly verified by our measurements.
2. The absolute magnitude of the measured losses is higher by approximately four times for both quartz and pyrex than the values predicted by theory. The degree of straightness of these tubes must influence this result greatly.

The second conclusion is supported in the following way. From reflectivity measurements we have experimentally verified the value of $Re(\nu_n)$ for pyrex and the result $Re(\nu_n) = 1.43$ agrees well with the values used in calculating the theoretical loss. Since we have ensured optimum coupling to EH_{11} the increased losses are not due to higher order modes. Finally, a calculation was performed to determine the



(a) Quartz.



(b) Pyrex tubing.

Fig. A-8. Measured waveguide losses for precision bore.

radius of curvature which could affect such an increase. The radii required are in the range of 25 m, where a 100-m radius indicates straightness to within 0.1 mm in 10 cm. Curvatures in this range are certainly not unreasonable for the tubes, which are obtained as precision bore tubes with only nominal straightness requirements.

Waveguide transmission measurements were also performed on actual laser structures of 1-mm bore BeO tubes. Table A-1 gives a description of the tubes studied and the measured transmission. Tube B1 had excellent transmission before and after the drilling of electrode holes from the side. By slightly misaligning the tube with respect to the input beam, we excited higher order modes. The transmission was again >99%, thus indicating that the waveguide losses must be quite small as expected from the theory¹ ($\alpha_{\text{theo}} = 4.3 \times 10^{-5} \text{ cm}$). Although it is difficult to draw direct conclusions from such data, some recommendations can be made that will facilitate laser performance. Transmission measurements must be made on all tubes to ensure cleanliness and straightness of the bore and to reduce the waveguide transmission. If, after the fabrication procedures are completed, good transmission (>99%) is measured, the performance of the laser should not be affected by waveguide losses.

TABLE A-1
Experimental Tubes and Measured Transmission

Tube	Description	% Transmission
B1a	8.5 cm, no electrodes	>99%
B1b	B1a, with 4 electrodes	>99%
B2	5 cm with 6 electrodes	96%
B3	8.6 cm, with 6 electrodes	97%
B4	1.4 cm, no electrodes	>99%

T1055

c. Rough Wall Waveguide Measurements - To determine directly the dependence of waveguide resonator losses on wall roughness a simple one-dimensional structure was used. Two pyrex glass plates (3 cm x 9 cm x 0.5 cm) were spaced 1/2 mm apart, thus defining a one dimensional waveguide structure. One of the glass plates was roughened by sandblasting. The surface roughness was measured with a Dektak profiler. From the measurement of transmission and using an assumed coupling figure of 95% for gaussian to TM conversion, an absolute α for both smooth and roughened waveguides was obtained.

Our previously derived expressions for the transmission of a roughened waveguide may be modified to describe the case where only one surface is roughened, giving

$$\ln T = -\frac{L}{2a \cot \phi} \ln rr'$$

where T is the transmission, $a = 0.5$ mm is the width of the guide, and r and r' are the reflectivities (at angle ϕ) for the smooth and roughened surfaces, respectively. Measured values of guide-transmission (as well as αL , r' , and r'/r) are given in Table A-II. For the smooth surface, we have $r' = 4$.

TABLE A-2

Transmission, Loss and Reflectivities for Three Structures

	T	αL	r'	r'/r
"Smooth"	0.805	0.220 cm^{-1}	0.942	1.0
SB 2	0.784	0.255	0.927	0.984
SB 5	0.708	0.35	0.876	0.930

T1395

According to Beckmann's theory for a normally distributed surface,

$$r'/r = e^{-\left(\frac{4\pi \sin \phi}{\lambda}\right)^2}$$

This allows us to calculate the rms roughness σ_{calc} from the measured values of r'/r and compare them with values of σ from Dektak measurements. We compare the calculated and measured values of σ for SB2 and SE5 in the following table.

	σ_{calc}	σ_{meas}
SB2	5 μm	8 μm
SB5	11	20

These results show that the calculated numbers are smaller than the measured values. This may be due to shadowing effects ($\sigma > \lambda$), which are not considered in Beckmann's analysis, or to inaccuracies in the determination of σ_{meas} from the Dektak plots.

However, the most important point established in this experiment is that SB2, which has a measured value of $\sigma = 8 \mu\text{m}$, still transmits 97.5% as much as the smooth walled waveguide. This 8 μm roughness is an order of magnitude larger than the measured roughness of the worst pyrex, quartz or even BeO waveguide candidates one might choose to implement in a laser. Here we have supporting experimental evidence for the contention that the wall roughness in the laser structures presently being made of BeO is of little consequence in determining laser performance.

REFERENCES

- A-1. E.A.J. Marcatili and R.A. Schmeltzer, Bell Syst. Tech. J. 43, 1783 (July 1974).
- A-2. R.L. Abrams and W.E. Bridges, IEEE J. Quantum Electron. QE-9, 940 (September 1973).
- A-3. P. Beckman, The Scattering of Electromagnetic Waves from Rough Surfaces (Macmillan, New York, 1963), Part 1.
- A-4. D. Marcuse, IEEE J. Quantum Electron. QE-8, 661 (July 1973).
- A-5. E. Loh, Phys. Rev. 166, 673 (February 1968).
- A-6. D.H. Hensler, Appl. Optics 11, 2522 (November 1973).
- A-7. R.L. Abrams, IEEE J. Quantum Electron. QE-8, 838 (November 1973).

APPENDIX B

The following paper will be published in the 1 Sept. 1974 issue of Applied Physics Letters.

GIGAHERTZ TUNABLE WAVEGUIDE CO₂ LASER*

R. L. Abrams
Hughes Research Laboratories
Malibu, California 90265

ABSTRACT

A sealed-off cw waveguide CO₂ laser has been continuously tuned over 1.2 GHz on a single transition at 10.6 μ m. The laser consists of a 9.5 cm x 1.0 mm square discharge tube fabricated from polished BeO slabs. Line selection is achieved with a diffraction grating and tuning is accomplished by piezoelectric control of the resonator length.

*The research reported in this paper was sponsored by the Advanced Research Projects Agency, monitored by the Office of Naval Research.

GIGAHERTZ TUNABLE WAVEGUIDE CO₂ LASER

Wideband tunable CO₂ lasers have been needed for a number of years for applications in laser communications, optical radar, pollution detection, and spectroscopy. The tuning range of a conventional low pressure CO₂ laser is limited by the relatively small Doppler width (~ 53 MHz) of the CO₂ laser transition. The development of the waveguide gas laser concept¹ and its extension² to high pressure, sealed-off, waveguide CO₂ lasers has resulted in pressure broadening of the laser transition and much larger available gain bandwidth for frequency tuning and other applications. This large bandwidth has been exploited for mode locking^{3,4} and is being considered for wideband power amplification.⁵ A high pressure waveguide CO₂ laser, with gas flow, was recently⁶ used to demonstrate a tunability over several hundred MHz. In this paper we discuss the demonstration of a tuning capability of 1.2 GHz on a single vibration-rotation transition in a sealed-off cw, waveguide CO₂ laser. Preliminary accounts of this work have been previously reported in Refs. 4 and 5.

At room temperature a typical CO₂ laser gas mixture is pressure broadened at a rate of ~ 5.3 MHz/Torr.⁷ Under laser discharge conditions, the gas temperature can rise to $\sim 400^\circ\text{K}$, which reduces the pressure broadening rate to ~ 4.5 MHz/Torr. Thus we find that pressures in the neighborhood of 200 to 300 Torr are necessary to achieve gigahertz tunability. Previous measurements on 1.5 mm i.d. sealed-off CO₂ laser discharges in both circular and square cross-section waveguides demonstrated the capability of laser oscillation at pressures above 300 Torr, with optimum laser output at a pressure of 150 Torr. Degnan⁸ has shown that, for a given resonator loss and output coupling, the gas pressure for optimum output power also results in maximum tunability. Thus, in order to achieve gigahertz tuning from a CO₂ laser, under optimum conditions, smaller discharge diameters and correspondingly higher pressures should be used.

It has been shown⁹ that BeO ceramic is the best available material for waveguide CO₂ lasers. Drilling of long, small radius holes through BeO can be accomplished, but this is a difficult and expensive process. In addition, the surface finish¹⁰ and straightness¹¹ of the hollow waveguide can strongly affect the waveguide transmission loss. For this reason, we have chosen to fabricate our waveguide lasers in a square geometry, allowing the use of polished BeO slabs. In this manner, we are assured of adequate surface finish and straightness.

The construction of the laser discharge tube is discussed with reference to Fig. B-1. The laser is fabricated from four polished BeO slabs, 9.5 cm long, epoxied together to form a 1.0 mm square waveguide. Copper gasketed vacuum flanges are machined to fit over the rectangular outer dimensions of the tube, and are epoxied to the ceramic. All subsequent hardware (mirror mounts, piezoelectric tuning element) is mounted by means of mating flanges. The electrodes consist of hollow nickel pins epoxied into countersunk holes in the ceramic. Four electrodes are used, allowing two independent discharge paths while maintaining the ends of the tube at ground potential. Evacuation and gas fill are provided by a feedthrough in one of the flanges. Cooling is achieved by conduction to a water-cooled aluminum heat sink.

The totally reflecting laser mirror is mounted on a bender bimorph, which is composed of two oppositely poled piezoelectric discs, bonded together. Application of a voltage across the bimorph causes a slight buckling, resulting in a linear mirror motion along the laser axis. Approximately 25 V are required to move the mirror one free spectral range (5.3 μm). The opposite end of the waveguide laser is fitted either with a flat output mirror or a 97% reflecting, 150 ℓ/mm , diffraction grating used in the Littrow configuration for line selection. In the latter case, output power is coupled off of the zeroth grating order, through a window in the mating flange. In addition, the polarizing properties of the grating insure oscillation on a linearly polarized resonator mode.

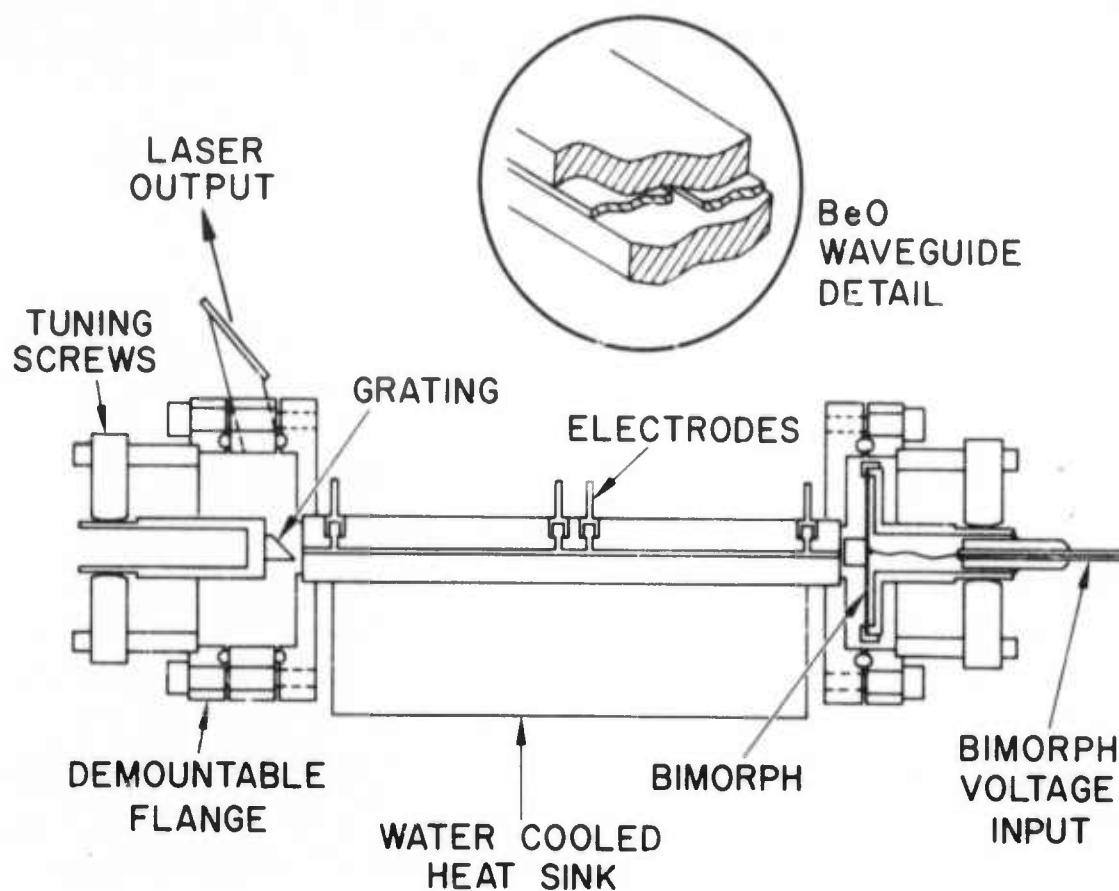


Fig. B-1. Tunable waveguide laser.

The waveguide laser was first fitted with a flat output mirror (96% reflecting, 3% transmission). Output power was then measured as a function of gas mixture and total pressure, with the results shown in Fig. B-2. The significance of the data is that optimum gas pressure is in the desirable 200 to 300 Torr region, rather than 150 Torr as found for 1.5 mm tubes.² The gas mixtures richer in helium operate most effectively at higher pressures, similar to the results in Ref. 2. In this case, however, laser action is observed at pressures in excess of 400 Torr.

When the output mirror was replaced with the 150 ℓ /mm diffraction grating, it was found that maximum tuning was achieved with an 8:1:0.5:0.25 mixture of He:CO₂:N₂:Xe. The grating was tuned for oscillation on the P(20), 00⁰₁ to 10⁰₀ transition at 10.59 μ m and output power was measured versus bimorph voltage (cavity length). The results are shown in Fig. B-3. The mirror separation is 9.8 cm, giving a cavity-free spectral range of 1530 MHz. The tuning range can be estimated from the fraction of a free spectral range over which oscillation is maintained on a single line. This tuning range was verified independently by a heterodyne measurement against a stable CO₂ laser. The maximum tuning was observed to be 1200 MHz at a static fill pressure of 260 Torr. Output power at the center of the line was 80 mW, limited by the small zeroth order grating reflectivity ($\sim 0.6\%$). For these conditions, laser tube voltage and current were 5.5 kV and 1.5 mA, respectively, through each section.

In another experiment, the total reflector was replaced by the grating (mounted on the bimorph) and the power output was taken from the 3% output mirror. In this case 500 mW was extracted from the laser at 260 Torr with a tuning range of 960 MHz. The tuning range is decreased due to the increased resonator loss, but the output power has increased significantly.

The theoretical tuning range can be estimated from the expression given by Degnan⁸

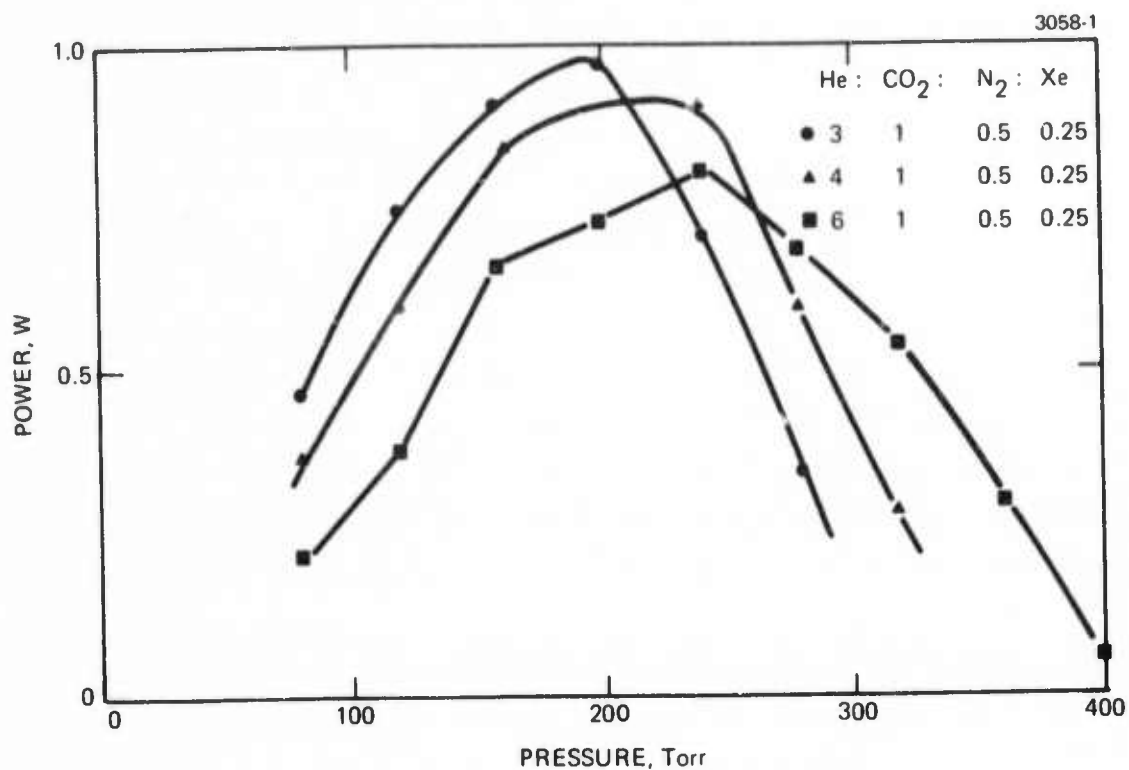


Fig. B-2. Output power from waveguide laser versus total pressure for several gas mixtures. Output is extracted from a 3% transmitting mirror ($R = 96\%$).

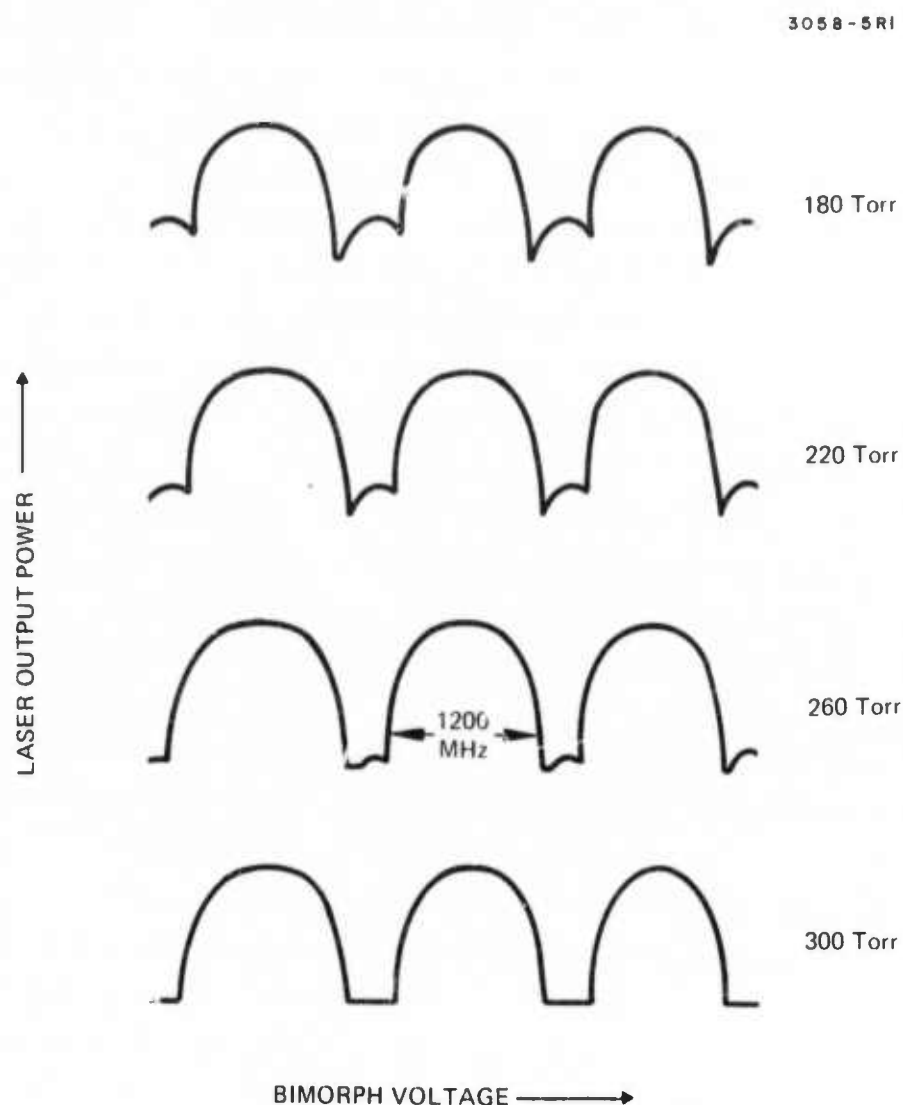


Fig. B-3. Tuning characteristics of waveguide laser for several values of total gas pressure. An 8:1:0.5:0.25 mixture of He:CO₂:N₂:Xe was used. Output power was coupled from the zeroth grating order and has a maximum value of 80 mW.

$$2|\nu_c - \nu_o| = \Delta\nu \left[\frac{g_o L}{\ln(1/\sqrt{r_1 r_2})} - 1 \right]^{1/2}$$

where $|\nu_c - \nu_o|$ is the tuning range from line center, g_o is the small signal gain coefficient at line center, L is the active laser length, and r_1 and r_2 are the reflectivities of the two mirrors. In our case, $r_1 = 0.99$, $r_2 = 0.97$, $\Delta\nu = 1170$ MHz at 260 Torr, and $L = 8.5$ cm. At these high pressures, if we assume $g_o = 0.005 \text{ cm}^{-1}$ (see Ref. 2), we calculate $2|\nu_c - \nu_o| = 1285$ MHz in reasonable agreement with the observed value. However, this agreement must be regarded as fortuitous, since the calculated value is sensitive to g_o (known only to $\sim 20\%$), and to the exact mirror reflectivities, and to waveguide losses which are assumed to be negligible here.

The frequency stability of a tunable waveguide laser has been measured by photomixing two of them together and observing the signal on a spectrum analyzer. The short term stability was ~ 100 kHz, limited by the acoustic environment in the laboratory. The FM noise spectrum was dominated by a narrow peak at 2.2 kHz, due to a mechanical resonance in the structure. With improved resonator design, we see no reason why these lasers should not offer the same type of stability observed with conventional CO_2 lasers.¹²

There would be considerable interest in extending this technique to smaller discharge diameters and thus higher operating pressures and larger tuning ranges. We have demonstrated comparable output power at correspondingly higher pressures from a 0.75 mm square bore tube of the same length. Since power per unit length should remain constant as the discharge diameter is decreased², this indicates that waveguide losses are not yet a significant factor. Attempts to tune this laser using a grating for line selection have not given the expected increase, however. This is probably due to an increased grating loss due to the small number of lines being illuminated over the 0.75 mm tube aperture. If line selection is obtained by an intracavity etalon or other resonant techniques, this may lead to increased tunability.

In conclusion, we have demonstrated a single line frequency tuning capability in excess of 1 GHz in a sealed-off, cw, waveguide CO₂ laser. Frequency stability measurements have shown the output to be reasonably stable, limited by mechanical resonance to ~100 kHz. The approach used here can be extended to smaller discharge diameters and higher pressures, but an alternate approach to line selection may be required.

The author would like to acknowledge numerous technical discussions with H.R. Friedrich, M.B. Klein, and G.L. Tangonan and the expert technical assistance of R.E. Brower.

REFERENCES

1. P.W. Smith, Appl. Phys. Lett. 19, 132 (1971).
2. R.L. Abrams and W.B. Bridges, IEEE J. of Quantum Electronics QE-9, 940 (1973).
3. P.W. Smith, T.J. Bridges, E.G. Burkhardt, and O.R. Wood, Appl. Phys. Lett. 21, 470 (1972).
4. R.L. Abrams, Conference on Laser Spectroscopy, Vail, CO (June 1973); 1973 NEREM Record, Boston, MA (Nov. 1973).
5. R.L. Abrams, Sixth DOD Conference on Laser Technology, U.S. Air Force Academy, Colorado Springs, CO (March 1974).
6. I.M. Beterov, V.P. Chebotayev, and A.S. Provorov, IEEE J. of Quantum Electronics, QE-10, 245 (1974).
7. R.L. Abrams, Appl. Phys. Lett. (to be published).
8. J.J. Degnan, J. Appl. Phys. 45, 257 (1974).
9. BeO is chosen for its excellent thermal conductivity as well as its superior dielectric properties as a 10.6 μm waveguide (see Ref. 2).
10. R.L. Abrams, Frequency Tuned CO_2 Laser, Interim Technical Report, ONR Contract N00014-73-C-0324.
11. E.A.J. Marcatili and R.A. Schmeltzer, Bell Syst. Tech. J. 43, 1783 (1964).
12. C. Freed, IEEE J. of Quantum Electronics QE-4, 404 (1968).



**HUGHES RESEARCH
LABORATORIES**

3011 MALIBU CANYON ROAD
MALIBU, CALIFORNIA • 90265